

Hadamard integrators for wave equations in time and frequency domain: Eulerian formulations via butterfly algorithms

Yuxiao Wei · Jin Cheng · Shingyu Leung · Robert Burrridge · Jianliang Qian

Received: date / Accepted: date

Abstract Starting from the Kirchhoff-Huygens representation and Duhamel's principle of time-domain wave equations, we propose novel butterfly-compressed Hadamard integrators for self-adjoint wave equations in both time and frequency domain in an inhomogeneous medium. First, we incorporate the leading term of Hadamard's ansatz into the Kirchhoff-Huygens representation to develop a short-time valid propagator. Second, using the Fourier transform in time, we derive the corresponding Eulerian short-time propagator in frequency domain; on top of this propagator, we further develop a time-frequency-time (TFT) method for the Cauchy problem of time-domain wave equations. Third, we further propose the time-frequency-time-frequency (TFTF) method for the corresponding point-source Helmholtz equation, which provides Green's functions of the Helmholtz equation for all angular frequencies within a given frequency band. Fourth, to implement TFT and TFTF methods efficiently, we introduce butterfly algorithms to compress oscillatory integral kernels at different frequencies. As a result, the proposed methods can construct wave field beyond caustics implicitly and advance spatially overturning waves in time naturally with quasi-optimal computational complexity and memory usage. Furthermore, once constructed the Hadamard integrators can be employed to solve both time-domain wave equations with various initial conditions and frequency-domain wave equations with different point sources. Numerical examples for two-dimensional wave equations illustrate the accuracy and efficiency of the proposed methods.

Keywords Time-dependent wave equation · Helmholtz equation · High frequency wave · Hadamard's ansatz · Butterfly algorithm · Caustics

Mathematics Subject Classification (2020) MSC 65M80 · MSC 65Y20

Cheng's research was supported by NSFC 11971121, 12241103 and the Sino-German Mobility Programme (M-0187) by the Sino-German Center for Research Promotion. S. Leung is supported by the Hong Kong RGC under grant 16302223. Qian's research is partially supported by NSF 2012046, 2152011, and 2309534.

Yuxiao Wei
E-mail: 19110180029@fudan.edu.cn ·
Jin Cheng
E-mail: jcheng@fudan.edu.cn ·
Shingyu Leung
E-mail: masyleung@ust.hk ·
Robert Burrridge
E-mail: burridge137@gmail.com ·
Jianliang Qian
E-mail: jqian@msu.edu

Yuxiao Wei · Jin Cheng
School of Mathematical Sciences, Fudan University, Shanghai 200433, China.

Shingyu Leung
Department of Mathematics, The Hong Kong University of Science and Technology, Clear Water Bay, Hong Kong.

Robert Burrridge
Department of Mathematics and Statistics, University of New Mexico, Albuquerque, NM 87131, USA.

Jianliang Qian
Department of Mathematics and Department of CMSE, Michigan State University, East Lansing, MI 48824, USA

1 Introduction

We consider the Cauchy problem for the self-adjoint wave equation in m -dimensional space \mathbb{R}^m ,

$$\rho u_{tt} - \nabla \cdot (\nu \nabla u) = f, \quad \mathbf{x} \in \mathbb{R}^m, \quad t > 0 \quad (1.1)$$

with initial conditions

$$u(0, \mathbf{x}) = u^1(\mathbf{x}), \quad u_t(0, \mathbf{x}) = u^2(\mathbf{x}), \quad (1.2)$$

where t is time, the subscripts t and tt represent the first and second time derivative, respectively, position $\mathbf{x} = [x_1, x_2, \dots, x_m]^T$, the gradient operator $\nabla = [\partial_{x_1}, \partial_{x_2}, \dots, \partial_{x_m}]^T$, both variables ρ and ν are analytic and positive functions of position \mathbf{x} , characterizing certain physical parameters of the medium, $f(t, \mathbf{x})$ is the source term, and $u^1(\mathbf{x})$ and $u^2(\mathbf{x})$ are compactly supported, highly oscillatory smooth functions.

Taking

$$f(t, \mathbf{x}) = \delta(t)\delta(\mathbf{x} - \mathbf{z}) \quad \text{and} \quad u^1 = u^2 = 0 \quad (1.3)$$

in equations (1.1) and (1.2) and applying the Fourier transform in time to equation (1.1) accordingly, we obtain the frequency-domain wave equation, the Helmholtz equation,

$$\nabla \cdot (\nu \nabla \hat{u}) + \omega^2 \rho \hat{u} = -\delta(\mathbf{x} - \mathbf{z}), \quad (1.4)$$

with the Sommerfeld radiation condition imposed at infinity, where ω is the angular frequency and \mathbf{z} is the source.

When the initial conditions in (1.2) are highly oscillatory or the angular frequency in (1.4) is large, the wave field will be highly oscillatory; however, direct numerical methods, such as finite-difference or finite-element methods, for such problems may suffer from dispersion or pollution errors [3, 5], so that such methods require an enormous computational grid to resolve these oscillations and are thus very costly in practice. Therefore, alternative methods, such as geometrical-optics based asymptotic methods, have been sought to resolve these highly-oscillatory wave phenomena.

To start with, we introduce Hadamard's ansatz [44] which is based on Gelfand and Shilov's family of generalized functions f_+^λ . It provides an asymptotic representation of the time-domain Green's function $G(t, \mathbf{x}_0; \mathbf{x})$ which satisfies the wave equation (1.1) with the source term $f = \delta(t)\delta(\mathbf{x} - \mathbf{x}_0)$ and initial conditions $u^1 = u^2 = 0$. On top of this ansatz, in [44] we have proposed a Lagrangian Hadamard integrator to solve the highly-oscillatory pure initial-value problem of the wave equation (1.1)-(1.2) with $f = 0$. It is noteworthy that although Hadamard's ansatz serves as a local short-time approximation for Green's functions before caustics occur, the Hadamard integrator can implicitly handle caustics by selecting a sufficiently small time step ΔT (which only depends on the medium) and recursively updating the wave field by marching forward in time with time step ΔT based on the Kirchhoff-Huygens representation. We denote by $\bar{T}(\mathbf{x}_0)$ the time when the first caustic occurs for rays issued from a source point \mathbf{x}_0 . For $\Delta T < \min_{\mathbf{x}_0 \in \Omega} \bar{T}(\mathbf{x}_0)$, where \mathbf{x}_0 is located in a certain bounded domain Ω , Hadamard's ansatz is valid in this domain Ω so that we can propagate wave forward in time with the time step ΔT using the Kirchhoff-Huygens representation. However, because the singularity of a Green's function $G(t, \mathbf{x}_0; \mathbf{x})$ is located on an irregular curved time-space wave front which yields integration over irregular curves in 2-D or surfaces in 3-D, it becomes challenging to minimize the computational complexity of the Lagrangian Hadamard integrator due to the required expensive integration over irregular wave fronts.

In this article, we derive Eulerian formulations for Gelfand-Shilov-function defined integrals arising from the Hadamard-Kirchhoff-Huygens (HKH) representation, leading to a short-time valid Eulerian HKH propagator for wave equations. Recursively utilizing this propagator results in an Eulerian Hadamard integrator for time-domain wave equations, where the Eulerian integrator, analogous to the Lagrangian integrator [44], is able to handle caustics implicitly and advance overturning waves naturally. Furthermore, in combination with the butterfly algorithm [24], the Eulerian Hadamard integrator can achieve quasi-linear computational complexity in both CPU time and memory usage, which is not achievable by the current Lagrangian Hadamard integrator [44]. Moreover, by further developing the methodology to tackle point-source singularities, we are also able to employ the Eulerian Hadamard integrator to solve the point-source Helmholtz equation in an inhomogeneous medium, where, once again, caustics are treated implicitly and overturning waves are advanced naturally.

The essential difficulty in developing Eulerian formulations of the HKH integrator is how to integrate the time-domain Green's function which has singularity on irregular curved wavefronts. Our strategy is based on the following two observations: (1) the time-domain Green's function of the wave equation is the inverse Fourier transform in time of the corresponding frequency-domain Green's function of the Helmholtz equation, and as shown in [35], each term in Hadamard's ansatz for the time-domain Green's

function is indeed the inverse Fourier transform in time of the corresponding term in Babich's ansatz [2, 27, 28] for the frequency-domain Green's function; (2) moreover, while the time-domain Green's function has singularity concentrated on irregular curved wavefronts which is unfriendly to numerical quadrature on regular mesh points, the frequency-domain Green's function only has singularity at the source point so that it is amenable to numerical quadrature on regular mesh points. These two observations motivate us to take a detour to apply the time-domain Green's function efficiently by first carrying out relevant actions in frequency domain and then coming back to time domain: first, take the Fourier transform in time to go to frequency domain; second, act the frequency-domain Green's function to corresponding arguments; third, take the inverse Fourier transform in frequency to get back to time domain.

Using the frequency-domain Green's function enables us to efficiently update the wave field $u(t, \mathbf{x})$ and its derivative $u_t(t, \mathbf{x})$, where the actions of the time derivatives of Green's function on test functions can be obtained through the Fourier transformation, leading to the time-frequency-time (TFT) method. Consequently, the TFT method converts singularities (of time-domain Green's functions) located on irregular wave fronts into those singularities (of frequency-domain Green's functions) located at regularly distributed source locations so that the computational complexity of matrix-vector multiplication formulated on regular mesh points can be further reduced by some matrix decomposition techniques.

Furthermore, with the help of the frequency-domain Green's function, solving the Cauchy problem (1.1)-(1.2) with the source term $f = 0$ and initial conditions $u^1(\mathbf{x}) = 0$ and $u^2(\mathbf{x}) = \frac{1}{\rho(\mathbf{x}_0)}\delta(\mathbf{x} - \mathbf{x}_0)$ and applying the inverse Fourier transform in time to the resulting time-domain solution $u(t, \mathbf{x})$, we obtain the frequency-domain solution $\hat{u}(\omega, \mathbf{x})$ to (1.4) for all angular frequencies within a specified frequency band, leading to the time-frequency-time-frequency (TFTF) method. A serious challenge arises here since the to-be-updated wave field, the time-domain Green's function, is a generalized function, and the corresponding Hadamard integrator makes it necessary to act a generalized function on another generalized function which may be *singular*¹. Thus we cannot use theoretical results that hold in the distributional sense, such as Fourier transforms, to calculate the actions of the time derivatives of Green's functions.

To overcome this challenge, we first utilize wave equations and integration by parts to transfer time derivatives of Green's functions $G(t, \mathbf{x}_0; \mathbf{x})$ to spatial derivatives of test functions. Subsequently, we employ a smooth approximation of the wave field at $T = \Delta T$, that is, a truncated Fourier summation of the frequency-domain Green's function, as the initial condition. Finally, we apply the TFT method to compute the action of the Green's function and update the wave field accordingly.

Then we immediately run into the question: How to efficiently apply the Eulerian Hadamard integrator in the TFT and TFTF method? Consider the two-dimensional ($m = 2$) wave equation with frequency bandwidth B , where the frequency bandwidth is implied by oscillatory initial conditions of the time-domain wave equation or the angular frequency range of the Helmholtz equation. By Shannon's sampling principle, we set spatial step $h = O(1/B)$ and time step $\Delta t = O(1/B)$ to generate a uniform discrete time-space mesh. To form the truncated Fourier series, we need to evaluate at least $O(B)$ integrals of frequency-domain Green's functions², where each numerical integral is equivalent to a matrix-vector multiplication of size $O(B^4)$. Thus a direct summation of truncated Fourier series will lead to $O(B)O(B^4) = O(B^5)$ complexity in both computational time and memory usage. Even if we only need a constant number of such frequency sampling steps and we can use fast Fourier transforms to obtain the corresponding time-domain solutions, the complexity of the entire algorithm will be at least $O(B^5)$, which is unacceptable for problems with only $O(B^3)$ unknowns, where the unknowns are defined in the time-space domain.

To accelerate the resulting matrix-vector multiplication in the TFT and TFTF method, we first construct the low-rank separable representations of the Hadamard ingredients including phase and Hadamard-coefficient functions by solving the corresponding governing equations and utilizing the Chebyshev expansion accordingly. Then we consider an algebraic compression tool called butterfly [6, 20, 21, 31], a multilevel numerical linear algebra algorithm well-suited for representing highly oscillatory operators, to compress the Hadamard integrator. We have applied the method in [24, 27, 29] to deal with the integral of Green's functions of the Helmholtz equation. For integral kernels with singularities that we are dealing with here, we combine hierarchical matrix representations and the butterfly algorithm by designing a suitable strategy for selecting proxy rows in the interpolation decomposition of butterfly construction, reducing the complexity of the matrix-vector multiplication to $O(B^2 \log^2(B))$. Thus, the overall CPU time and memory usage of the butterfly compressed Hadamard integrator scale as $O(B^3 \log^2(B))$ for the two-dimensional time-domain wave equation, where the proportionality constant depends only on the

¹ Generalized functions whose actions can be given by integrals of certain locally summable generic functions are called *regular*, and all others are called *singular*.

² Here by the integration or integral of a Green's function, we mean the integral of the product of a Green's function and a sufficiently well-behaved function.

specified accuracy and is independent of the frequency parameter B ; since solving the two-dimensional time-domain wave equation is in fact equivalent to solving a three-dimensional (1-D in time and 2-D in space) problem, we have the cubic power in B in the complexity estimate, which is quasi-optimal.

It is important to note that the Hadamard integrator is independent of initial conditions. Once constructed, it can be used to solve both time-domain wave equations with various initial conditions and frequency-domain wave equations with different point sources. Moreover, once these butterfly decompositions are constructed, these butterfly representations can be applied recursively when executing the Hadamard integrator; this unique feature allows the Hadamard integrator to be efficiently parallelized.

1.1 Related works

Geometrical-optics-based asymptotic methods have been widely used to resolve highly oscillatory wave phenomena, and the critical question is how to construct the global wave field in the presence of caustics. One approach is to replace the geometrical-optics ansatz with Gaussian beam (GB) summations [4, 34, 38, 39, 42, 43]. Eulerian formulations of GB summations have been developed for Helmholtz equations in the high-frequency regime [15, 17, 19] and the time-dependent Schrödinger equations [16]. The main challenge of this approach is that the computations have to be done in the high-dimensional phase space. Another approach is to incorporate the geometrical-optics ansatz into the Huygens secondary-source principle, resulting in fast Huygens sweeping (FHS) methods, and these methods have been designed to solve time-dependent Schrödinger equations [11, 18], Helmholtz equations [27, 29], frequency-domain Maxwell's equations [28, 33], time-harmonic vectorial Maxwell's equations [14], and frequency-domain elastic wave equations [36], all in the presence of caustics. FHS methods are able to propagate wave fields through appropriately partitioned spatial layers by marching in that preferred spatial direction in a layer-by-layer fashion, but these methods only work in media where geodesics satisfy the sub-horizontal condition [41]. Based on Hadamard's ansatz for the time-domain Green's function which is inspired by the Hadamard method [7, 10], a Lagrangian Hadamard integrator is designed in [44] to propagate wave fields by marching in time direction without assuming the sub-horizontal condition on geodesics; moreover, the advantages of the Lagrangian integrator are twofold: it not only can handle caustics implicitly but also can advance overturning waves naturally. However, due to the singularity of Hadamard's ansatz at irregular wave fronts, it is hard for the Lagrangian Hadamard integrator in [44] to achieve a quasi-linear computational complexity.

Our Eulerian Hadamard integrator inherits the advantages of the Lagrangian Hadamard integrator in [44] by marching in time direction; moreover, since the Eulerian integrator has relied on the butterfly algorithm to speed up the matrix-vector multiplication arising from integration process, the computational complexity of the Eulerian integrator for the wave equation in both time and frequency domain can be reduced to quasi-linear. Moreover, our Eulerian Hadamard integrator is also able to solve the point-source Helmholtz equation in inhomogeneous media by treating caustics implicitly and handling overturning waves naturally, thus settling the issue of how to remove the sub-horizontal condition in the fast Huygens sweeping methods [27–29, 33] so that overturning waves can be propagated.

1.2 Layout of the paper

We introduce in Section 2 the Kirchhoff-Huygens representation formula which utilizes Green's functions to propagate waves. Connecting Hadamard's ansatz and Babich's ansatz using Fourier transform, we propose in Section 3 novel Eulerian Hadamard-Kirchhoff-Huygens (HKH) propagators for the Cauchy problem of the time-dependent wave equation and the point-source problem of the frequency-dependent wave equation, and we further obtain the Eulerian Hadamard integrators by applying them recursively. We then develop in Section 4 numerical strategies for implementing the Eulerian Hadamard integrators. To accelerate the constructions and applications of the integrators, in Section 5 we construct interpolative decomposition butterfly (IDBF) and hierarchically off-diagonal butterfly (HODBF) representations of the integral kernels, resulting in quasi-optimal computational complexity and memory usage. Section 6 presents two-dimensional (2-D) results to demonstrate the accuracy, efficiency and convergence of the proposed methods. We conclude the paper with some comments in Section 7.

2 Kirchhoff-Huygens representation formula

We are interested in solving the Cauchy problem for the self-adjoint wave equation (1.1) with initial conditions (1.2). Let $S(t)$ be the solution operator corresponding to $f = 0$ and $u^1 = 0$; namely, for a function ψ , $u(t, \mathbf{x}) = (S(t)\psi)(\mathbf{x})$ solves (1.1) with the source term $f = 0$ and the initial conditions $u^1 = 0$ and $u^2 = \psi$. Then Duhamel's principle implies that the solution for wave equation (1.1) with initial conditions (1.2) is

$$u(t, \mathbf{x}_0) = \partial_t(S(t)u^1)(\mathbf{x}_0) + (S(t)u^2)(\mathbf{x}_0) + \int_0^t (S(t-s)f(s, \cdot))(\mathbf{x}_0)ds. \quad (2.1)$$

Consider the time-domain Green's function $G(t, \mathbf{x}_0; \mathbf{x})$ which satisfies (1.1) with the source term and initial conditions specified in (1.3). Then, for a compactly supported function ψ such that the initial condition $u^2 = \psi$, by [44] the solution operator S can be written as

$$(S(t)\psi)(\mathbf{x}_0) = \int_V \rho(\mathbf{x})G(t, \mathbf{x}_0; \mathbf{x})\psi(\mathbf{x})d\mathbf{x}, \quad (2.2)$$

where V is a region of space which contains the support of ψ and does not change in time.

Then we have

$$u(t, \mathbf{x}_0) = \int_V \rho(\mathbf{x})[G_t(t, \mathbf{x}_0; \mathbf{x})u^1(\mathbf{x}) + G(t, \mathbf{x}_0; \mathbf{x})u^2(\mathbf{x})]d\mathbf{x} + \int_0^t \int_V \rho(\mathbf{x})G(t-s, \mathbf{x}_0; \mathbf{x})f(s, \mathbf{x})d\mathbf{x}ds. \quad (2.3)$$

Differentiating (2.3) with respect to t , we obtain

$$u_t(t, \mathbf{x}_0) = \int_V \rho(\mathbf{x})[G_{tt}(t, \mathbf{x}_0; \mathbf{x})u^1(\mathbf{x}) + G_t(t, \mathbf{x}_0; \mathbf{x})u^2(\mathbf{x})]d\mathbf{x} + \int_0^t \int_V \rho(\mathbf{x})G_t(t-s, \mathbf{x}_0; \mathbf{x})f(s, \mathbf{x})d\mathbf{x}ds. \quad (2.4)$$

We refer to (2.3) and (2.4) as the Kirchhoff-Huygens representation formula. When the medium is homogeneous, Green's function for the wave equation is known so that the formula has been used frequently in practice. When the medium is inhomogeneous and the source term $f = 0$, in [44] we have used Hadamard's ansatz to compute the needed Green's function for the formula, leading to a short-time valid propagator in a Lagrangian formulation, dubbed the Hadamard-Kirchhoff-Huygens (HKH) propagator, which is able to propagate a highly oscillatory wave field for a short period of time; furthermore, a Lagrangian Hadamard integrator is obtained by recursively applying the HKH propagator in time. In this article, we continue to use Hadamard's ansatz to construct Green's functions in the Kirchhoff-Huygens formula, but we compute the HKH propagator using an Eulerian formulation, resulting in an Eulerian Hadamard integrator.

To simplify the presentation, in the current work we only consider the two-dimensional case, where $m = 2$, and we leave the three-dimensional case as a future work. Consequently, we consider the following two cases:

- Case 1. The pure initial-value problem for equation (1.1), where $f = 0$, and u^1 and u^2 are compactly supported, highly oscillatory smooth functions.
- Case 2. The point-source problem for equation (1.4), where the frequency-domain Green's function of the Helmholtz equation naturally corresponds to the time-domain Green's function of the wave equation (1.1) with $f = \delta(t)\delta(\mathbf{x} - \mathbf{x}_0)$ and $u^1 = u^2 = 0$.

In Case 1 for pure initial-value problems, we employ the same setup as in [44], aiming to achieve quasi-optimal computational complexity using Eulerian formulations.

In Case 2 for point-source problems of the Helmholtz equation, since the time-domain Green's function corresponding to $f = \delta(t)\delta(\mathbf{x} - \mathbf{x}_0)$ and $u^1 = u^2 = 0$ in the Cauchy problem (1.1)-(1.2) is naturally linked to the frequency-domain Green's function of the Helmholtz equation, we extend the Hadamard integrator to point-source wave equations in frequency domain so as to solve the point-source Helmholtz equation. Because the Hadamard integrator marches in the time direction, it can naturally handle overturning waves in frequency domain, which is in sharp contrast to our previous frequency-domain asymptotic methods in [27, 29], in that the methods in [27, 29] are not able to treat overturning waves.

On the other hand, for a generic source term $f(x, t) \neq 0$ with compact support in both space and time, the Kirchhoff-Huygens representation (2.3)-(2.4) contains a volume integral of $m + 1$ dimension, which is expensive to evaluate; therefore, we leave this as a future work as well.

3 Eulerian HKH propagator

3.1 Hadamard's ansatz for time-domain Green's functions

Consider Green's function of the self-adjoint wave equation

$$\rho u_{tt} - \nabla \cdot (\nu \nabla u) = \delta(t) \delta(\mathbf{x} - \mathbf{x}_0), \quad \mathbf{x} \in \mathbb{R}^m, \quad t > 0 \quad (3.1)$$

with initial conditions

$$u(0, \mathbf{x}) = 0, \quad u_t(0, \mathbf{x}) = 0. \quad (3.2)$$

Let

$$c = \sqrt{\frac{\nu}{\rho}}, \quad n = \frac{1}{c} = \sqrt{\frac{\rho}{\nu}}. \quad (3.3)$$

Then Hadamard's ansatz [44] is written as

$$u(t, \mathbf{x}_0; \mathbf{x}) = \sum_{s=0}^{\infty} v_s(\mathbf{x}_0; \mathbf{x}) f_+^{s-\frac{m-1}{2}} [t^2 - \tau^2(\mathbf{x}_0; \mathbf{x})], \quad (3.4)$$

where the Gelfand-Shilov generalized functions $f_+^\lambda(\zeta)$ are given in [9]. They are defined for $\lambda > -1$ as follows:

$$f_+^\lambda(\zeta) = \frac{\zeta_+^\lambda}{\lambda!}, \quad (3.5)$$

where

$$\zeta_+^\lambda = \begin{cases} 0, & \text{for } \zeta < 0, \\ \zeta^\lambda, & \text{otherwise,} \end{cases} \quad (3.6)$$

and by analytic continuation for other values of λ ; in particular, $\lambda = 0$ corresponds to the Heaviside function, yielding the jump discontinuity at $\zeta = 0$, whereas $\lambda = -1$ corresponds to the δ -function. Here $\tau(\mathbf{x}_0; \mathbf{x})$ is the phase function, also known as traveltime, satisfying the eikonal equation (3.7),

$$|\nabla \tau| = n, \quad \tau(\mathbf{x}_0; \mathbf{x})|_{\mathbf{x}=\mathbf{x}_0} = 0. \quad (3.7)$$

And the coefficient functions $v_s(\mathbf{x}_0; \mathbf{x})$ in (3.4) satisfy the recurrent system

$$4\rho\tau \frac{dv_s}{d\tau} + v_s [\nabla \cdot (\nu \nabla \tau^2) + 2(2s - m)\rho] = \nabla \cdot (\nu \nabla v_{s-1}), \quad s = 0, 1, 2, \dots, \quad (3.8)$$

and $v_{-1} \equiv 0$. By leveraging properties of the Gelfand-Shilov function as demonstrated in [44], we have the initial condition for v_0 at \mathbf{x}_0 :

$$v_0(\mathbf{x}_0; \mathbf{x})|_{\mathbf{x}=\mathbf{x}_0} = \frac{n^m(\mathbf{x}_0)}{2\rho(\mathbf{x}_0)\pi^{\frac{m-1}{2}}} = \frac{n^{m-2}(\mathbf{x}_0)}{2\nu(\mathbf{x}_0)\pi^{\frac{m-1}{2}}}. \quad (3.9)$$

We introduce some definitions and properties of generalized functions [9] here. We first denote K the space of test functions which consists of all real functions $\phi(\mathbf{x})$ with continuous derivatives of all orders and with bounded support. We next define a generalized function as any linear continuous functional on K . These functionals (generalized functions) which can be given by an equation such as

$$(\Psi, \phi) = \int_{R^n} \Psi(\mathbf{x}) \phi(\mathbf{x}) d\mathbf{x} \quad \text{for } \forall \phi \in K \quad (3.10)$$

with Ψ an absolutely integrable in every bounded region of R^n shall be called regular, and all others (including the delta function) will be called singular. It's worth noting that $f_+^\lambda(\zeta)$ is regular when $\lambda > -1$ and singular when $\lambda \leq -1$.

3.2 Babich's ansatz for frequency-domain Green's functions

In order to develop Eulerian formulations, we introduce Babich's ansatz [2, 27, 28, 33] for the frequency-domain Green's function $\hat{u} = \hat{G}(\omega, \mathbf{x}_0; \mathbf{x})$ of the Helmholtz equation (1.4), which is written as

$$\hat{u}(\omega, \mathbf{x}_0; \mathbf{x}) = \hat{G}(\omega, \mathbf{x}_0; \mathbf{x}) = \sum_{s=0}^{\infty} v_s(\mathbf{x}_0; \mathbf{x}) f_{s+1-\frac{m}{2}}(\tau(\mathbf{x}_0; \mathbf{x}), \omega), \quad (3.11)$$

where τ still represents the traveltime, v_s represent the coefficient functions,

$$f_p(\tau, \omega) = i \frac{\sqrt{\pi}}{2} e^{ip\pi} \left(\frac{2\tau}{\omega} \right)^p H_p^{(1)}(\omega\tau) = i \frac{\sqrt{\pi}}{2} \left(\frac{2\tau}{\omega} \right)^p H_{-p}^{(1)}(\omega\tau), \quad (3.12)$$

and $H_p^{(1)}$ is the p -th Hankel function of the first kind. In [27], using properties of the basis $f_p(\tau, \omega)$, we have obtained that τ satisfies the eikonal equation (3.7) and v_s satisfy the recurrent system (3.8) with the initial condition (3.9). That is, the time-independent phase and coefficient functions in Hadamard's ansatz are the same as the frequency-independent phase and coefficient functions in Babich's ansatz. Furthermore, [28] shows that the basis functions of Hadamard's ansatz and Babich's ansatz are linked to each other:

$$\int_{\tau}^{\infty} e^{i\omega t} f_+^{(\nu-\frac{1}{2})}(t^2 - \tau^2(\mathbf{x}_0; \mathbf{x})) dt = \frac{1}{2} i \sqrt{\pi} \left(\frac{2\tau}{\omega} \right)^{\nu} e^{i\omega\tau} H_{\nu}^{(1)}(\omega\tau) \equiv f_{\nu}(\omega, \tau). \quad (3.13)$$

Because of the reciprocity, we have $\hat{G}(\omega, \mathbf{x}_0; \mathbf{x}) = \hat{G}(\omega, \mathbf{x}; \mathbf{x}_0)$, which will be used frequently in the following algorithmic development. Letting $G_0(t, \mathbf{x}_0; \mathbf{x})$ and $\hat{G}_0(\omega, \mathbf{x}_0; \mathbf{x})$ be the leading term of Hadamard's ansatz (3.4) and Babich's ansatz (3.11), respectively, for a point source located at \mathbf{x}_0 , we have the following crucial relations,

$$G_0(t, \mathbf{x}_0; \mathbf{x}) = \frac{1}{2\pi} \int_{-\infty}^{\infty} \hat{G}_0(\omega, \mathbf{x}_0; \mathbf{x}) e^{-i\omega t} d\omega = \frac{1}{\pi} \Re \left[\int_0^{\infty} \hat{G}_0(\omega, \mathbf{x}_0; \mathbf{x}) e^{-i\omega t} d\omega \right], \quad (3.14)$$

where \Re represents the real part, and

$$\hat{G}_0(\omega, \mathbf{x}_0; \mathbf{x}) = \int_0^{\infty} G_0(t, \mathbf{x}_0; \mathbf{x}) e^{i\omega t} dt, \quad (3.15)$$

where $G_0(t, \mathbf{x}_0; \mathbf{x})|_{t<0} \equiv 0$.

This observation inspires us to replace the time-domain Green's function with a truncated finite-bandwidth Fourier summation of the frequency-domain Green's function, where the singularities of the time-domain Green's function are naturally transferred to the singularities at source points of the frequency-domain Green's function, resulting in the time-frequency-time (TFT) method for Case 1 and the time-frequency-time-frequency (TFTF) method for Case 2, as alluded to in Section 2.

3.3 Eulerian formulations: the TFT method for Case 1

Now we start with developing the TFT method for Case 1, where $f \equiv 0$, and u^1 and u^2 are compactly supported, highly oscillatory smooth functions, and we will compute the integrals of G_0 , \dot{G}_0 and \ddot{G}_0 , respectively, where, by the integration or integral of a Green's function, we mean the integral of the product of a Green's function and a sufficiently well-behaved function.

First, we apply the time-domain Green's function to $\phi(\mathbf{x})$, a test function in the space K as defined above, and use (3.14) to obtain

$$\begin{aligned} \int_{V_{\mathbf{x}_0}} G_0(t, \mathbf{x}_0; \mathbf{x}) \phi(\mathbf{x}) d\mathbf{x} &= \int_{V_{\mathbf{x}_0}} \frac{1}{\pi} \int_{-\infty}^{\infty} e^{-i\omega t} \hat{G}_0(\omega, \mathbf{x}_0; \mathbf{x}) d\omega \phi(\mathbf{x}) d\mathbf{x} \\ &= \frac{1}{2\pi} \int_{-\infty}^{\infty} \int_{V_{\mathbf{x}_0}} \hat{G}_0(\omega, \mathbf{x}_0; \mathbf{x}) \phi(\mathbf{x}) d\mathbf{x} e^{-i\omega t} d\omega \\ &= \frac{1}{\pi} \Re \left[\int_0^{\infty} \int_{V_{\mathbf{x}_0}} \hat{G}_0(\omega, \mathbf{x}_0; \mathbf{x}) \phi(\mathbf{x}) d\mathbf{x} e^{-i\omega t} d\omega \right]. \end{aligned} \quad (3.16)$$

Here $V_{\mathbf{x}_0}$ is an integration region independent of time t , satisfying

$$V_{\mathbf{x}_0} \supseteq \{\mathbf{x} : \tau < t_0\} \supseteq \{\mathbf{x} : \tau < \Delta T\}, \quad (3.17)$$

where t_0 is a constant that depends on the medium and satisfies $t < \Delta T < t_0 < \bar{T}(\mathbf{x}_0)$.

Differentiating (3.16) with respect to t in the distributional sense, we can realize the action of $\dot{G}_0(t, \mathbf{x}_0; \mathbf{x})$ in frequency domain as the following

$$\begin{aligned} \int_{V_{\mathbf{x}_0}} \dot{G}_0(t, \mathbf{x}_0; \mathbf{x}) \phi(\mathbf{x}) d\mathbf{x} &= \int_{V_{\mathbf{x}_0}} \frac{1}{2\pi} \int_{-\infty}^{\infty} (-i\omega) \hat{G}_0(\omega, \mathbf{x}_0; \mathbf{x}) e^{-i\omega t} d\omega \phi(\mathbf{x}) d\mathbf{x} \\ &= \frac{1}{2\pi} \int_{-\infty}^{\infty} (-i\omega) \int_{V_{\mathbf{x}_0}} \hat{G}_0(\omega, \mathbf{x}_0; \mathbf{x}) \phi(\mathbf{x}) d\mathbf{x} e^{-i\omega t} d\omega \\ &= \frac{1}{\pi} \Re \left[\int_0^{\infty} (-i\omega) \int_{V_{\mathbf{x}_0}} \hat{G}_0(\omega, \mathbf{x}_0; \mathbf{x}) \phi(\mathbf{x}) d\mathbf{x} e^{-i\omega t} d\omega \right]. \end{aligned} \quad (3.18)$$

Further differentiating (3.18) with respect to t in the distributional sense, we have

$$\begin{aligned} \int_{V_{\mathbf{x}_0}} \ddot{G}_0(t, \mathbf{x}_0; \mathbf{x}) \phi(\mathbf{x}) d\mathbf{x} &= \int_{V_{\mathbf{x}_0}} \frac{1}{2\pi} \int_{-\infty}^{\infty} (-i\omega)^2 \hat{G}_0(\omega, \mathbf{x}_0; \mathbf{x}) e^{-i\omega t} d\omega \phi(\mathbf{x}) d\mathbf{x} \\ &= \frac{1}{\pi} \Re \left[\int_0^{\infty} (-i\omega)^2 \int_{V_{\mathbf{x}_0}} \hat{G}_0(\omega, \mathbf{x}_0; \mathbf{x}) \phi(\mathbf{x}) d\mathbf{x} e^{-i\omega t} d\omega \right]. \end{aligned} \quad (3.19)$$

Then, by taking $\phi(\mathbf{x})$ as $\rho(\mathbf{x})u^1(\mathbf{x})$ and $\rho(\mathbf{x})u^2(\mathbf{x})$, respectively, in the Kirchhoff-Huygens representation formulas (2.3)-(2.4), we have the following Eulerian formulations,

$$\begin{aligned} u(t, \mathbf{x}_0) &= \int_{V_{\mathbf{x}_0}} \dot{G}_0(t, \mathbf{x}_0; \mathbf{x}) u^1(\mathbf{x}) + \rho(\mathbf{x}) \dot{G}_0(t, \mathbf{x}_0; \mathbf{x}) u^2(\mathbf{x}) d\mathbf{x} \\ &= \frac{1}{\pi} \Re \left[\int_0^{\infty} (i\omega) \int_{V_{\mathbf{x}_0}} \hat{G}_0(\omega, \mathbf{x}_0; \mathbf{x}) \rho u^1 d\mathbf{x} e^{-i\omega t} d\omega \right] \\ &\quad + \frac{1}{\pi} \Re \left[\int_0^{\infty} \int_{V_{\mathbf{x}_0}} \hat{G}_0(\omega, \mathbf{x}_0; \mathbf{x}) \rho u^2 d\mathbf{x} e^{-i\omega t} d\omega \right], \end{aligned} \quad (3.20)$$

and

$$\begin{aligned} u_t(t, \mathbf{x}_0) &= \int_{V_{\mathbf{x}_0}} \ddot{G}_0(t, \mathbf{x}_0; \mathbf{x}) u^1(\mathbf{x}) + \rho(\mathbf{x}) \ddot{G}_0(t, \mathbf{x}_0; \mathbf{x}) u^2(\mathbf{x}) d\mathbf{x} \\ &= \frac{1}{\pi} \Re \left[\int_0^{\infty} (i\omega)^2 \int_{V_{\mathbf{x}_0}} \hat{G}_0(\omega, \mathbf{x}_0; \mathbf{x}) \rho u^1 d\mathbf{x} e^{-i\omega t} d\omega \right] \\ &\quad + \frac{1}{\pi} \Re \left[\int_0^{\infty} (i\omega) \int_{V_{\mathbf{x}_0}} \hat{G}_0(\omega, \mathbf{x}_0; \mathbf{x}) \rho u^2 d\mathbf{x} e^{-i\omega t} d\omega \right]. \end{aligned} \quad (3.21)$$

Since the frequency-domain Green's function is only singular at the source point which is amenable to Eulerian evaluation on uniform meshes, we refer to (3.20)-(3.21) as the Eulerian Hadamard-Kirchhoff-Huygens (HKH) propagator for the TFFT method, which is used to propagate the wave field from $\tau = 0$ to $\tau = t$, where $0 < t < \bar{T}$. Although the HKH-TFFT propagator is only valid for a short-time period in a caustic-free neighborhood, recursively applying this propagator in time yields the *TFFT Eulerian Hadamard integrator* to solve time-dependent wave equations globally in time, where caustics are treated implicitly and spatially overturning waves are handled naturally in *time domain*.

3.4 Eulerian formulations: the TFFT method for Case 2

Now we develop the TFFT method for Case 2, point-source problems for the Helmholtz equation by first solving the corresponding time-domain wave equations and then applying the inverse Fourier transform in time to the resulting time-domain solutions.

According to Duhamel's principle, we can rewrite the corresponding time-domain wave equation of the point-source Helmholtz equation (1.4) in the same form as Case 1,

$$\rho(\mathbf{x})u_{tt}(t, \mathbf{x}) - \nabla \cdot [\nu(\mathbf{x})\nabla u(t, \mathbf{x})] = 0 \quad \text{for } t > 0, \quad (3.22)$$

with initial conditions

$$u(0, \mathbf{x}) = 0 \quad \text{and} \quad u_t(0, \mathbf{x}) = \frac{1}{\rho(\mathbf{z})} \delta(\mathbf{x} - \mathbf{z}). \quad (3.23)$$

The challenge arises from the fact that the wave solution in Case 2 is the time-domain Green's function, a generalized function. In each time step, we need to numerically act generalized functions on other generalized functions. Specifically, with the initial conditions at $T = 0$ containing the singular generalized function δ , we have

$$u(t, \mathbf{x}_0) = \int \rho(\mathbf{x})G(t, \mathbf{x}_0; \mathbf{x}) \frac{\delta(\mathbf{x} - \mathbf{z})}{\rho(\mathbf{z})} d\mathbf{x} = G(t, \mathbf{x}_0; \mathbf{z}) \quad (3.24)$$

and

$$u_t(t, \mathbf{x}_0) = \int \rho(\mathbf{x})G_t(t, \mathbf{x}_0; \mathbf{x}) \frac{\delta(\mathbf{x} - \mathbf{z})}{\rho(\mathbf{z})} d\mathbf{x} = G_t(t, \mathbf{x}_0; \mathbf{z}) \quad (3.25)$$

in the *distributional sense*. Since $G_t(t, \mathbf{x}_0; \mathbf{z})$ is *singular*, no locally summable generic function is available that can be used to update $u_t(t, \mathbf{x}_0)$; consequently, equations (3.18) and (3.19), which only hold in the distributional sense, no longer hold in the current setting.

To overcome this challenge, we employ a two-step strategy: first, we use integration by parts to convert the time derivative of Green's function into the spatial derivative of the test function; second, instead of initializing at $T = 0$ using the singular delta function, we initialize the wave field at $T = \Delta T$ with a smooth approximation, which is obtained by truncating the Fourier summation of the frequency-domain Green's function.

To start with, we follow [44] to introduce the geodesic (ray) polar transformation for a given source \mathbf{x}_0 :

$$P[\mathbf{x}_0] : \mathbf{x} \rightarrow (\tau, \boldsymbol{\omega}), \quad (3.26)$$

where τ is traveltime, $\boldsymbol{\omega} \in \mathbb{S}^{m-1}$ is take-off angle of a ray, and $(\tau, \boldsymbol{\omega})$ is the geodesic polar coordinates. Within any neighborhood of \mathbf{x}_0 not containing any caustics other than \mathbf{x}_0 , there is one and only one ray connecting \mathbf{x} and \mathbf{x}_0 , which means $P[\mathbf{x}_0]$ is well-defined and one-to-one, and \mathbf{x} is a smooth function of the point $\mathbf{y} = \mathbf{x}_0 + \tau\boldsymbol{\omega}$. To facilitate our following discussions, we also write down the volume element as the following,

$$d\mathbf{x} = ds dS = c d\tau dS = c \left| \frac{\partial S}{\partial \boldsymbol{\omega}} \right| d\tau d\boldsymbol{\omega}, \quad (3.27)$$

where s is the arc length along the ray, $dS = \left| \frac{\partial S}{\partial \boldsymbol{\omega}} \right| d\boldsymbol{\omega}$ is the element of area cut out on the wave front $\tau = \text{const.}$ by rays emanated from the solid angle element $d\boldsymbol{\omega}$ at the source. According to the appendix of [44], we have

$$\left| \frac{\partial S}{\partial \boldsymbol{\omega}} \right| = \frac{\tau^{m-1}}{4\rho_0 c_0^m \pi^{m-1} \rho c v_0^2}, \quad (3.28)$$

where $\rho_0 = \rho(\mathbf{x}_0)$ and $c_0 = c(\mathbf{x}_0)$.

We now apply $\dot{G}(t, \mathbf{x}_0; \mathbf{x})$ to a test function $\phi(\mathbf{x}) \in K$ and use the geodesic polar transformation and its inverse,

$$\begin{aligned}
\int \dot{G}(t, \mathbf{x}_0; \mathbf{x}) \phi(\mathbf{x}) d\mathbf{x} &= 2t \int f_+^{-\frac{1}{2}-1} [t^2 - \tau^2] v_0(\mathbf{x}) \phi(\mathbf{x}) d\mathbf{x} \\
&= 2t \int \left(-\frac{\partial}{2\tau \partial \tau} \right) f_+^{-\frac{1}{2}} [t^2 - \tau^2] v_0 \phi d\mathbf{x} \\
&= 2t \int_0^{2\pi} \int_0^t \left(-\frac{\partial}{2\tau \partial \tau} \right) f_+^{-\frac{1}{2}} [t^2 - \tau^2] v_0 \phi \left| \frac{\partial S}{\partial \boldsymbol{\omega}} \right| c d\tau d\theta \\
&= t \int_0^{2\pi} \left[f_+^{-\frac{1}{2}} [t^2 - \tau^2] \frac{\phi}{4\rho_0 c_0^2 \pi \rho v_0} \right]_{\tau=t}^0 d\theta \\
&\quad + t \int_0^{2\pi} \int_0^t f_+^{-\frac{1}{2}} [t^2 - \tau^2] \left(\frac{\partial}{\partial \tau} \right) \left[\frac{\phi}{4\rho_0 c_0^2 \pi \rho v_0} \right] d\tau d\theta \\
&= \frac{\phi(\mathbf{x}_0)}{\rho(\mathbf{x}_0)} + t \int_0^{2\pi} \int_0^t G_0(t, \mathbf{x}_0; \mathbf{x}) \frac{1}{v_0} \left(\frac{\partial}{\partial \tau} \right) \left[\frac{\phi}{4\rho_0 c_0^2 \pi \rho v_0} \right] d\tau d\theta \\
&= \frac{\phi(\mathbf{x}_0)}{\rho(\mathbf{x}_0)} + t \int_{V_{\mathbf{x}_0}} G_0(t, \mathbf{x}_0; \mathbf{x}) \frac{1}{v_0} \left(\frac{\partial}{\partial \tau} \right) \left[\frac{\phi}{4\rho_0 c_0^2 \pi \rho v_0} \right] \frac{1}{c \left| \frac{\partial S}{\partial \boldsymbol{\omega}} \right|} d\mathbf{x} \\
&= \frac{\phi(\mathbf{x}_0)}{\rho(\mathbf{x}_0)} + t \int_{V_{\mathbf{x}_0}} G_0(t, \mathbf{x}_0; \mathbf{x}) \left(\frac{\partial}{\partial \tau} \right) \left[\frac{\phi}{\rho v_0} \right] \frac{\rho}{\tau} d\mathbf{x},
\end{aligned} \tag{3.29}$$

where θ is the take-off angle $\boldsymbol{\omega}$ when $m = 2$, and we have used (3.28), (3.9) and $f_+^\lambda[0] = 0$. Further using (3.16), we have

$$\int \dot{G}_0(t, \mathbf{x}_0; \mathbf{x}) \phi(\mathbf{x}) d\mathbf{x} = \frac{\phi(\mathbf{x}_0)}{\rho(\mathbf{x}_0)} + \frac{t}{\pi} \Re \left[\int_0^\infty e^{-i\omega t} \int_{V_{\mathbf{x}_0}} \hat{G}_0(\omega, \mathbf{x}_0; \mathbf{x}) \left(\frac{\partial}{\partial \tau} \right) \left[\frac{\phi}{\rho v_0} \right] \frac{\rho v_0}{\tau} d\mathbf{x} d\omega \right]. \tag{3.30}$$

Here the the directional derivative

$$\frac{\partial}{\partial \tau} = c^2 \nabla \tau \cdot \nabla, \tag{3.31}$$

is obtained by utilizing the method of characteristics to solve the eikonal equation (3.7).

As for \ddot{G}_0 , for $t > 0$, we have

$$\rho \ddot{G}_0(t, \mathbf{x}_0; \mathbf{x}) - \nabla \cdot (\nu \nabla G_0(t, \mathbf{x}_0; \mathbf{x})) = 0. \tag{3.32}$$

Applying $\ddot{G}_0(t, \mathbf{x}_0; \mathbf{x})$ to a test function $\phi(\mathbf{x})$ and using integration by parts and (3.16), we have

$$\begin{aligned}
\int_{V_{\mathbf{x}_0}} \ddot{G}_0(t, \mathbf{x}_0; \mathbf{x}) \phi(\mathbf{x}) d\mathbf{x} &= \int_{V_{\mathbf{x}_0}} \nabla \cdot (\nu \nabla G_0(t, \mathbf{x}_0; \mathbf{x})) \frac{\phi}{\rho} d\mathbf{x} \\
&= \int G_0(t, \mathbf{x}_0; \mathbf{x}) \nabla \cdot (\nu \nabla \frac{\phi}{\rho}) d\mathbf{x} \\
&= \frac{1}{\pi} \Re \left[\int_0^\infty \int_{V_{\mathbf{x}_0}} \hat{G}_0(\omega, \mathbf{x}_0; \mathbf{x}) \nabla \cdot (\nu \nabla \frac{\phi}{\rho}) d\mathbf{x} e^{-i\omega t} d\omega \right].
\end{aligned} \tag{3.33}$$

Now, taking $\phi(\mathbf{x})$ as $\rho(\mathbf{x})u^1(\mathbf{x})$ and $\rho(\mathbf{x})u^2(\mathbf{x})$, respectively, in the Kirchhoff-Huygens representation formulas (2.3)-(2.4), we obtain the following Eulerian formulations,

$$\begin{aligned}
u(t, \mathbf{x}_0) &= u^1(\mathbf{x}_0) + \frac{1}{\pi} \Re \left[\int_0^\infty \int_{V_{\mathbf{x}_0}} \hat{G}_0(\omega, \mathbf{x}_0; \mathbf{x}) \rho u^2(\mathbf{x}) d\mathbf{x} e^{-i\omega t} d\omega \right] \\
&\quad + \frac{t}{\pi} \Re \left[\int_0^\infty \int_{V_{\mathbf{x}_0}} \hat{G}_0(\omega, \mathbf{x}_0; \mathbf{x}) \left(\frac{\partial}{\partial \tau} \right) \left(\frac{u^1}{v_0} \right) \frac{\rho v_0}{\tau} d\mathbf{x} e^{-i\omega t} d\omega \right],
\end{aligned} \tag{3.34}$$

and

$$\begin{aligned}
u_t(t, \mathbf{x}_0) &= u^2(\mathbf{x}_0) + \frac{t}{\pi} \Re \left[\int_0^\infty \int_{V_{\mathbf{x}_0}} \hat{G}_0(\omega, \mathbf{x}_0; \mathbf{x}) \left(\frac{\partial}{\partial \tau} \right) \left(\frac{u^2}{v_0} \right) \frac{\rho v_0}{\tau} d\mathbf{x} e^{-i\omega t} d\omega \right] \\
&\quad + \frac{1}{\pi} \Re \left[\int_0^\infty \int_{V_{\mathbf{x}_0}} \hat{G}_0(\omega, \mathbf{x}_0; \mathbf{x}) \nabla \cdot (\nu \nabla u^1) d\mathbf{x} e^{-i\omega t} d\omega \right].
\end{aligned} \tag{3.35}$$

We refer to (3.34)-(3.35) as the Eulerian Hadamard-Kirchhoff-Huygens (HKH) propagator for the TFTF method, which is used to propagate the wave field in time domain from $\tau = 0$ to $\tau = t$, where $0 < t < \bar{T}$. Although the HKH-TFTF propagator is only valid for a short-time period in a caustic-free neighborhood, recursively applying this propagator in time yields the global time-domain Green's function. Further we can utilize the inverse Fourier transform to get the frequency-domain solution $\hat{u}(\omega, \mathbf{x})$

$$\hat{u}(\omega, \mathbf{x}) = \int_0^\infty e^{i\omega t} u(t, \mathbf{x}) dt, \quad (3.36)$$

leading to the *TFTF Eulerian Hadamard integrator* to solve frequency-domain point-source wave equations (point-source Helmholtz equations) globally in time and thus globally in space, where the latter (“globally in space”) is implied by the eikonal-defined traveltimes function.

Consequently, the TFTF Eulerian Hadamard integrator is able to treat caustics implicitly and handle spatially overturning waves naturally in *frequency domain*.

4 Numerics for Eulerian Hadamard integrators

We present numerics for implementing TFT and TFTF Eulerian Hadamard integrators. We will design Eulerian methods to numerically discretize the HKH propagator so as to obtain the corresponding Eulerian Hadamard integrators by recursively applying the propagator in time. For highly oscillatory wave fields, we maintain a fixed number of points per wavelength (PPW) to uniformly discretize the computational domain into regular grid points.

To start with, we briefly discuss higher-order sweeping schemes for the eikonal and transport equations, yielding the squared-phase function τ^2 and the Hadamard coefficient v_0 , respectively. Subsequently, the low-rank representations based on Chebyshev interpolation are introduced to compress those smooth ingredients used in the HKH propagators. Finally, we present preliminary algorithms for implementing TFT and TFTF Eulerian Hadamard integrators.

4.1 Hadamard ingredients

In order to form the HKH propagators (3.20)-(3.21) and (3.34)-(3.35), we need to compute some ingredients corresponding to τ and v_0 , including

$$\tau, v_0, \nabla\tau, \nabla\tau \cdot \nabla v_0. \quad (4.1)$$

Since τ^2 rather than τ is smooth at source points, we obtain smooth representations for the following quantities:

$$\tau^2, v_0, \nabla\tau^2, \nabla\tau^2 \cdot \nabla v_0, \quad (4.2)$$

which can be transformed back to (4.1) via dividing by $\sqrt{\tau^2}$. We refer to the ingredients in (4.2) as Hadamard ingredients.

τ^2 and v_0 are obtained by solving the eikonal equation (3.7) first and the transport equation (3.8) afterwards. $\nabla\tau^2$ is obtained by a proper finite-difference method. As for $\nabla\tau^2 \cdot \nabla v_0$, instead of using finite differencing which may reduce accuracy, we again use the transport equation (3.8) to obtain

$$\nabla\tau^2 \cdot \nabla v_0 = \frac{2m\rho v_0 - \nabla \cdot [\nu \nabla\tau^2] v_0}{2\nu}. \quad (4.3)$$

4.2 Numerical schemes

The leading-order term of the Hadamard ansatz is defined by two functions, the eikonal τ satisfying the eikonal equation (3.7) and the Hadamard coefficient v_0 satisfying the transport equation (3.8). Since we have assumed that the Hadamard ansatz is valid locally around the source point, we need access to these two functions in order to construct the ansatz. Since the eikonal equation as a first-order nonlinear partial differential equation does not have analytical solutions in general, we have to use a robust, high-order numerical scheme to numerically solve this equation; moreover, the eikonal equation equipped with a point-source condition is even more tricky to deal with due to the upwind singularity at the source point [37]. To make the situation even more complicated, the transport equation (3.8) for the Hadamard

coefficient v_0 is weakly coupled with the eikonal equation (3.7) in that the coefficients of the former equation depend on the solution of the latter.

Fortunately, this set of weakly coupled equations with point-source conditions has been solved to high-order accuracy by using Lax-Friedrichs weighted essentially non-oscillatory (LxF-WENO) sweeping schemes as demonstrated in [40]. The high-order schemes in [40] have adopted essential ideas from many sources including [8, 12, 13, 22, 27, 30, 32, 37, 45, 46] and have been used in many applications. Consequently, we will adopt these schemes to our setting as well and we omit details here.

4.3 Multivariate Low-rank representation

The Hadamard ingredients (4.1) are time independent. According to [40], if variable functions ρ and ν are analytic, then τ^2 and v_0 are analytic in the region of space containing a point source but no other caustics. Consider two regions Ω_S and Ω_R with $\Omega_S \subset \Omega_R$ such that rays originated from any $\mathbf{x}_0 \in \Omega_S$ will not intersect in Ω_R , which means that no caustics will develop in Ω_R ; consequently, $\tau^2(\mathbf{x}_0; \mathbf{x})$ and $v_0(\mathbf{x}_0; \mathbf{x})$ are analytic in $\Omega_S \times \Omega_R$ so that we can construct Chebyshev-polynomials based low-rank representations of Hadamard ingredients with respect to both \mathbf{x}_0 and \mathbf{x} [24, 26–28].

Letting $f(x, y, x_0, y_0) = \tau^2, v_0, \frac{\partial \tau^2}{\partial x}, \frac{\partial \tau^2}{\partial y}, \nabla \tau^2 \cdot \nabla v_0$, respectively, we consider the following analytical low-rank representation using Chebyshev interpolation,

$$f(x, y, x_0, y_0) \approx \sum_{i=1}^{n_i} \sum_{j=1}^{n_0} \sum_{k=1}^{n_k} \sum_{l=1}^{n_l} F(i, j, k, l) \bar{T}_i(x) \bar{T}_j(y) \bar{T}_k(x_0) \bar{T}_l(y_0), \quad (4.4)$$

where n_i, n_0, n_k , and n_l are the orders of Chebyshev interpolation, F is a 4-D tensor of size $n_i \times n_j \times n_k \times n_l$ which contains the spectral coefficients to be determined, and $\bar{T}_i, \bar{T}_j, \bar{T}_k$, and \bar{T}_l represent the Chebyshev interpolants defined via translating the standard Chebyshev polynomials T_m defined on $[-1, 1]$ to the corresponding domain,

$$T_m(s) = \cos(m \arccos(s)), \quad s \in [-1, 1]. \quad (4.5)$$

We can obtain F by applying fast cosine transforms with respect to x, y, x_0 , and y_0 to the tensor $f(x_i^c, y_j^c, x_{0,k}^c, y_{0,l}^c)$, where $x_i^c, y_j^c, x_{0,k}^c$, and $y_{0,l}^c$ are n_i, n_j, n_k , and n_l -order Chebyshev nodes in $\Omega_R \times \Omega_S$, respectively, which are also obtained by translating the Chebyshev nodes $\{s_m\}$ in $[-1, 1]$,

$$s_m = \cos\left(\frac{2m-1}{2n_m}\right), \quad m = 1, 2, \dots, n_m. \quad (4.6)$$

To calculate $f(x_i^c, y_j^c, x_{0,k}^c, y_{0,l}^c)$, we adopt a computational strategy as used in [24]: we first choose a region Ω_c which is slightly larger than Ω_R and on which the ingredients are still analytic, then compute numerically the ingredients in Ω_R with sources located at $(x_{0,k}^c, y_{0,l}^c)$, respectively, and use cubic spline interpolation of the just computed ingredients on uniform grids to obtain $f(x_i^c, y_j^c, x_{0,k}^c, y_{0,l}^c)$.

After obtaining F , we can evaluate $f(x, y, x_0, y_0)$ at any point $(x, y, x_0, y_0) \in \Omega_S \times \Omega_R$ using (4.4), and the evaluation can be further accelerated by partial summation [29]. So far, we have finished the pre-computation and compression of the Hadamard ingredients in $\Omega_R \times \Omega_S$ so that the integral kernels can be constructed by assembling these ingredients into the Hadamard's or Babich's ansatz.

Different from marching along a spatial direction [27], when we use the Hadamard integrator to march in time direction, we always take Ω_S as a subset of Ω_R . Actually, for given caustic-free regions Ω_S and Ω_R , the maximum time step is bounded by the minimum traveltime

$$\tau_{\min} = \min_{\mathbf{x}_0 \in \partial\Omega_S, \mathbf{x} \in \partial\Omega_R} \tau(\mathbf{x}_0; \mathbf{x}). \quad (4.7)$$

We do not need to obtain the strict upper bound. Instead, we can determine the time step by dividing the minimum distance between $\partial\Omega_S$ and $\partial\Omega_R$ by the maximum wave speed $\max c$. Due to possible caustics in an inhomogeneous medium, we need to partition the computational domain Ω into several Ω_S^ℓ and the corresponding Ω_R^ℓ such that we can utilize the locally valid short-time HKH propagator to update the wave fields in Ω_S^ℓ via the information in Ω_R^ℓ , separately. The partitioning of regions and the time step only depend on the medium.

4.4 Numerical discretization

To numerically implement the HKH propagators, we shall first truncate the infinite frequency-domain integration interval $[0, \infty]$ with an artificial frequency domain bandwidth B that is problem specific in the sense that the bandwidth depends on the highly-oscillatory initial conditions in Case 1 and on the angular frequency ω in Case 2.

4.4.1 HKH-TFT propagator

In the TFT method, once the oscillatory initial conditions (1.2) are given, the wave solution is essentially bandlimited in the sense that the frequency information of the corresponding wave solution is determined and decays rapidly outside a certain frequency band. Thus we can select a sufficiently large artificial frequency domain bandwidth B to truncate the Fourier integral in frequency, where fast decay ensures that truncation does not introduce significant truncation errors.

After truncating the frequency domain, we uniformly discretize the frequency interval $[0, B]$ into

$$\{\omega_k : \omega_k = (k + \frac{1}{2})\Delta\omega, k = 0, 1, 2, \dots, N_\omega - 1\}, \quad (4.8)$$

where $B = N_\omega \Delta\omega$. Since the frequency-domain Green's function $\hat{G}_0(\omega, \mathbf{x}_0; \mathbf{x})$ in the two-dimensional case has logarithmic singularity when $\omega\tau \rightarrow 0$,

$$\hat{G}_0(\omega, \mathbf{x}_0; \mathbf{x}) \sim \frac{\sqrt{\pi}}{2} v_0 \frac{2}{\pi} \ln(\omega\tau) \quad \text{as } \omega\tau \rightarrow 0, \quad (4.9)$$

we need to treat the integrals of $\hat{G}_0(\omega, \mathbf{x}_0; \mathbf{x})$ over $[0, \Delta\omega]$ with caution.

Now we discretize the HKH-TFT propagator in the frequency domain as follows,

$$\begin{aligned} u(t, \mathbf{x}_0) &\approx \frac{\Delta\omega}{\pi} \Re \left[\sum_{k=0}^{N_\omega-1} (i\omega_k) e^{-i\omega_k t} \int_{V_{\mathbf{x}_0}} \hat{G}_0(\omega_k, \mathbf{x}_0; \mathbf{x}) \rho u^1 d\mathbf{x} \right] \\ &+ \frac{\Delta\omega}{\pi} \Re \left[\sum_{k=1}^{N_\omega-1} e^{-i\omega_k t} \int_{V_{\mathbf{x}_0}} \hat{G}_0(\omega_k, \mathbf{x}_0; \mathbf{x}) \rho u^2 d\mathbf{x} \right] \\ &+ \frac{1}{\pi} \Re \left[\int_{V_{\mathbf{x}_0}} \int_0^{\Delta\omega} \hat{G}_0(\omega, \mathbf{x}_0; \mathbf{x}) \rho u^2 e^{-i\omega t} d\omega d\mathbf{x} \right], \end{aligned} \quad (4.10)$$

and

$$\begin{aligned} u_t(t, \mathbf{x}_0) &\approx \frac{\Delta\omega}{\pi} \Re \left[\sum_{k=0}^{N_\omega-1} (i\omega_k)^2 e^{-i\omega_k t} \int_{V_{\mathbf{x}_0}} \hat{G}_0(\omega_k, \mathbf{x}_0; \mathbf{x}) \rho u^1 d\mathbf{x} \right] \\ &+ \frac{\Delta\omega}{\pi} \Re \left[\sum_{k=0}^{N_\omega-1} (i\omega_k) e^{-i\omega_k t} \int_{V_{\mathbf{x}_0}} \hat{G}_0(\omega_k, \mathbf{x}_0; \mathbf{x}) \rho u^2 d\mathbf{x} \right]. \end{aligned} \quad (4.11)$$

Before we further discretize the propagator in space, we need to deal with the frequency-space integral

$$\int_{V_{\mathbf{x}_0}} \int_0^{\Delta\omega} e^{-i\omega t} \hat{G}_0(\omega, \mathbf{x}_0; \mathbf{x}) d\omega \psi(\mathbf{x}_0; \mathbf{x}) d\mathbf{x}, \quad (4.12)$$

where $\psi(\mathbf{x}_0; \mathbf{x})$ represents the frequency-independent part of the integrand in the HKH propagator. The difficulty comes from the singularity of the frequency-domain Green's function when $\omega \rightarrow 0$. However, since τ has a small upper bound that only depends on the medium, we have $\omega\tau \sim 0$; we thus use the polynomial approximation of the Hankel function $H_0^1(\omega\tau)$ [1] to approximate the kernel \hat{G}_0 so that

$$I(t, \mathbf{x}_0; \mathbf{x}) \doteq \int_0^{\Delta\omega} e^{-i\omega t} \hat{G}_0(\omega, \mathbf{x}_0; \mathbf{x}) d\omega \quad (4.13)$$

can be evaluated, and the technical details can be found in Appendix A.1. Then integral (4.12) can be rewritten as an action of time-dependent kernel $I(t, \mathbf{x}_0; \mathbf{x})$

$$\int_{V_{\mathbf{x}_0}} \int_0^{\Delta\omega} e^{-i\omega t} \hat{G}_0(\omega, \mathbf{x}_0; \mathbf{x}) d\omega \psi(\mathbf{x}_0; \mathbf{x}) d\mathbf{x} = \int_{V_{\mathbf{x}_0}} I(t, \mathbf{x}_0; \mathbf{x}) \psi(\mathbf{x}_0; \mathbf{x}) d\mathbf{x}. \quad (4.14)$$

We now discretize the HKH-TFT propagator in space. Consider a source region Ω_S and the corresponding receiver region Ω_R which are uniformly discretized into N and M grid points, respectively. Then, a key issue is how to evaluate the self-interaction (diagonal) terms of the kernels, where $\hat{G}_0(\omega, \mathbf{x}_0; \mathbf{x})$ and $I(t, \mathbf{x}_0; \mathbf{x})$ are singular at $\mathbf{x} = \mathbf{x}_0$. After uniformly discretizing the computational regions, the diagonal terms can be replaced by integral averages over a cell centered at \mathbf{x}_0 , where the non-singular parts of the integrand are treated as constants. Letting c_j be the cell of size h centered at \mathbf{x}_0 , the Appendix of [24] provides

$$\begin{aligned}\hat{G}_0(\omega, \mathbf{x}_0; \mathbf{x}_0) &\doteq \frac{1}{h^2} \int_{c_j} \hat{G}_0(\omega, \mathbf{x}_0; \mathbf{x}) d\mathbf{x} \\ &\approx \frac{i}{(2hn_0\omega)^2} \left[8 \int_0^{\frac{\pi}{4}} \frac{hn_0\omega}{2\cos\theta} H_1^{(1)}\left(\frac{hn_0\omega}{2\cos\theta}\right) d\theta + 4i \right],\end{aligned}\quad (4.15)$$

where $n_0 = n(\mathbf{x}_0)$. Based on (4.15), we further derive the approximation for

$$I(t, \mathbf{x}_0; \mathbf{x}_0) \doteq \frac{1}{h^2} \int_{c_j} \int_0^{\Delta\omega} e^{-i\omega t} \hat{G}_0(\omega, \mathbf{x}_0; \mathbf{x}) d\omega d\mathbf{x} \quad (4.16)$$

in Appendix A.2, where we have used the polynomial approximation of the Hankel function $H_1^{(1)}$.

At this point, we can define the frequency-dependent kernels

$$U_1^\omega = [(U_1^\omega)_{i,j}] = [\hat{G}_0(\omega, \mathbf{x}_0^i; \mathbf{x}_0^j)]_{1 \leq i \leq N, 1 \leq j \leq M}, \quad (4.17)$$

and the corresponding time-dependent kernels

$$\check{U}_1^t = [(\check{U}_1^t)_{i,j}] = \left[\int_0^{\Delta\omega} e^{i\omega t} U_1^\omega(\mathbf{x}_0^i; \mathbf{x}_0^j) d\omega \right]_{1 \leq i \leq N, 1 \leq j \leq M}. \quad (4.18)$$

Further, we define vectors

$$\begin{aligned}f_1 &= [\rho(\mathbf{x}^1)u^2(\mathbf{x}^1), \quad \dots, \quad \rho(\mathbf{x}^M)u^2(\mathbf{x}^M)]^T, \\ f_9 &= [\rho(\mathbf{x}^1)u^1(\mathbf{x}^1), \quad \dots, \quad \rho(\mathbf{x}^M)u^1(\mathbf{x}^M)]^T.\end{aligned}\quad (4.19)$$

We then introduce the frequency-sampling functions of size $N \times 1$ for $0 \leq k \leq N_\omega$

$$\begin{aligned}\hat{u}_1(\omega_k) &= U_1^{\omega_k} f_1, \\ \hat{u}_5(\omega_k) &= U_1^{\omega_k} f_9,\end{aligned}\quad (4.20)$$

and the time-sampling functions of size $N \times 1$ for $0 < t_\ell \leq \Delta T$

$$\check{u}_1(t_\ell) = \check{U}_1^{t_\ell} f_1, \quad (4.21)$$

Once we obtain all the above sampling functions, according to (3.20) and (3.21), we update $u(t_\ell, \mathbf{x}_0)$ and $u_t(t_\ell, \mathbf{x}_0)$ for all $0 < t_\ell \leq \Delta T$ and $\mathbf{x}_0 \in \Omega_S$ as

$$u(t_\ell, \mathbf{x}_0) \approx \frac{1}{\pi} \Re \left[\check{u}_1(t_\ell) + \Delta\omega \sum_{k=1}^{N_\omega-1} e^{-i\omega_k t_\ell} \hat{u}_1(\omega_k) + \Delta\omega \sum_{k=0}^{N_\omega-1} (-i\omega_k) e^{-i\omega_k t_\ell} \hat{u}_5(\omega_k) \right] \quad (4.22)$$

and

$$u_t(t_\ell, \mathbf{x}_0) \approx \frac{1}{\pi} \Re \left[\Delta\omega \sum_{k=0}^{N_\omega-1} (-i\omega_k) e^{-i\omega_k t_\ell} \hat{u}_1(\omega_k) + \Delta\omega \sum_{k=0}^{N_\omega-1} (-i\omega_k)^2 e^{-i\omega_k t_\ell} \hat{u}_5(\omega_k) \right]. \quad (4.23)$$

4.4.2 HKH-TFTF propagator

In the TFTF method, the bandwidth $B = \kappa\omega$ is selected according to the angular frequency ω , where κ is the oversampling parameter.

Using asymptotic properties of Hankel functions [1], for $m = 2$, we have for the frequency-domain Green's function,

$$\hat{G}_0(\omega, \mathbf{x}_0; \mathbf{x}) \sim i \frac{\sqrt{\pi}}{2} v_0 \sqrt{\frac{2}{\pi\omega\tau}} e^{i\omega\tau - \frac{\pi}{4}} \quad \text{as } \omega\tau \rightarrow \infty, \quad (4.24)$$

which does not decay rapidly.

Hence, large truncation errors may occur when we reconstruct the wave solution by

$$G_0(t, \mathbf{x}_0; \mathbf{x}) = \Re \left[\int_0^\infty e^{-i\omega t} \hat{G}_0(\omega, \mathbf{x}_0; \mathbf{x}) d\omega \right] \approx \Re \left[\int_0^B e^{-i\omega t} \hat{G}_0(\omega, \mathbf{x}_0; \mathbf{x}) d\omega \right]. \quad (4.25)$$

For fixed t and $\mathbf{x} \in \{\mathbf{x} : \tau(\mathbf{x}_0; \mathbf{x}) \neq t\}$, $e^{-i\omega t} \hat{G}_0(\omega, \mathbf{x}_0; \mathbf{x})$ is oscillatory and decays at $O(\frac{1}{\sqrt{\omega}})$. Therefore, truncation of (4.25) to bandwidth B will introduce the truncation error of no more than $O(\frac{1}{\sqrt{B}})$.

Consequently, we discretize the HKH-TFTF propagator in the frequency domain as follows,

$$\begin{aligned} u(t, \mathbf{x}_0) &\approx u^1(\mathbf{x}_0) + \frac{1}{\pi} \Re \left[\int_0^{\Delta\omega} \int_{V_{\mathbf{x}_0}} \hat{G}_0(\omega, \mathbf{x}_0; \mathbf{x}) \rho u^2(\mathbf{x}) d\mathbf{x} e^{-i\omega t} d\omega \right] \\ &\quad + \frac{\Delta\omega}{\pi} \Re \left[\sum_{k=1}^{N_\omega-1} e^{-i\omega_k t} \int_{V_{\mathbf{x}_0}} \hat{G}_0(\omega_k, \mathbf{x}_0; \mathbf{x}) \rho u^2(\mathbf{x}) d\mathbf{x} \right] \\ &\quad + \frac{t}{\pi} \Re \left[\int_0^{\Delta\omega} \int_{V_{\mathbf{x}_0}} \hat{G}_0(\omega, \mathbf{x}_0; \mathbf{x}) \left(\frac{\partial}{\partial\tau} \right) \left(\frac{u^1}{v_0} \right) \frac{\rho v_0}{\tau} d\mathbf{x} e^{-i\omega t} d\omega \right] \\ &\quad + \frac{t\Delta\omega}{\pi} \Re \left[\sum_{k=1}^{N_\omega-1} e^{-i\omega_k t} \int_{V_{\mathbf{x}_0}} \hat{G}_0(\omega_k, \mathbf{x}_0; \mathbf{x}) \left(\frac{\partial}{\partial\tau} \right) \left(\frac{u^1}{v_0} \right) \frac{\rho v_0}{\tau} d\mathbf{x} \right], \end{aligned} \quad (4.26)$$

and

$$\begin{aligned} u_t(t, \mathbf{x}_0) &\approx u^2(\mathbf{x}_0) + \frac{t}{\pi} \Re \left[\int_0^{\Delta\omega} \int_{V_{\mathbf{x}_0}} \hat{G}_0(\omega, \mathbf{x}_0; \mathbf{x}) \left(\frac{\partial}{\partial\tau} \right) \left(\frac{u^2}{v_0} \right) \frac{\rho v_0}{\tau} d\mathbf{x} e^{-i\omega t} d\omega \right] \\ &\quad + \frac{t\Delta\omega}{\pi} \Re \left[\sum_{k=1}^{N_\omega-1} e^{-i\omega_k t} \int_{V_{\mathbf{x}_0}} \hat{G}_0(\omega_k, \mathbf{x}_0; \mathbf{x}) \left(\frac{\partial}{\partial\tau} \right) \left(\frac{u^2}{v_0} \right) \frac{\rho v_0}{\tau} d\mathbf{x} \right] \\ &\quad + \frac{1}{\pi} \Re \left[\int_0^{\Delta\omega} \int_{V_{\mathbf{x}_0}} \hat{G}_0(\omega, \mathbf{x}_0; \mathbf{x}) \nabla \cdot (\nu \nabla u^1) d\mathbf{x} e^{-i\omega t} d\omega \right] \\ &\quad + \frac{\Delta\omega}{\pi} \Re \left[\sum_{k=1}^{N_\omega-1} e^{-i\omega_k t} \int_{V_{\mathbf{x}_0}} \hat{G}_0(\omega_k, \mathbf{x}_0; \mathbf{x}) \nabla \cdot (\nu \nabla u^1) d\mathbf{x} \right]. \end{aligned} \quad (4.27)$$

Here we utilize the same techniques as in the HKH-TFT propagator to handle frequency-space integrals (4.12) and the diagonal terms $\hat{G}_0(\omega, \mathbf{x}_0; \mathbf{x}_0)$ and $I(t, \mathbf{x}_0; \mathbf{x}_0)$. Furthermore, we need to consider the following additional diagonal terms.

The first diagonal term is

$$\left[\hat{G}_0(\omega, \mathbf{x}_0; \mathbf{x}) \frac{\partial}{\tau \partial\tau} \left(\frac{u^k}{v_0} \right) \right] \Big|_{\mathbf{x}=\mathbf{x}_0}, \quad k = 1, 2, \quad (4.28)$$

and the second diagonal term is

$$\left[\int_0^{\Delta\omega} e^{-i\omega t} \hat{G}_0(\omega, \mathbf{x}_0; \mathbf{x}) \frac{\partial}{\tau \partial\tau} \left(\frac{u^k}{v_0} \right) d\omega \right] \Big|_{\mathbf{x}=\mathbf{x}_0}, \quad k = 1, 2. \quad (4.29)$$

We can utilize the symmetry of $\frac{\partial}{\partial\tau} = c^2 \nabla \tau \cdot \nabla$ to obtain

$$\begin{aligned} &\left[\hat{G}_0(\omega, \mathbf{x}_0; \mathbf{x}) \frac{\partial}{\tau \partial\tau} \left(\frac{u^k}{v_0} \right) \right] \Big|_{\mathbf{x}=\mathbf{x}_0} \\ &\doteq \frac{1}{h^2} \int_{c_j} \left[\hat{G}_0(\omega, \mathbf{x}_0; \mathbf{x}) \frac{\partial}{\tau \partial\tau} \left(\frac{u^k}{v_0} \right) \right] d\mathbf{x} = 0, \quad k = 1, 2, \end{aligned} \quad (4.30)$$

and the details can be found in Appendix A.3.

Multiplying (4.30) by $e^{-i\omega t}$, we integrate the resulting formula over $[0, \Delta\omega]$ to compute the second diagonal term, leading to

$$\begin{aligned} & \left[\int_0^{\Delta\omega} e^{-i\omega t} \hat{G}_0(\omega, \mathbf{x}_0; \mathbf{x}) \frac{\partial}{\partial \tau} \left(\frac{u^k}{v_0} \right) d\omega \right] \Big|_{\mathbf{x}=\mathbf{x}_0} \\ & \doteq \frac{1}{h^2} \int_{c_j} \int_0^{\Delta\omega} e^{-i\omega t} \hat{G}_0(\omega, \mathbf{x}_0; \mathbf{x}) d\omega \frac{\partial}{\partial \tau} \left(\frac{u^k}{v_0} \right) d\mathbf{x} = 0, \quad k = 1, 2. \end{aligned} \quad (4.31)$$

Finally, we discretize the HKH-TFTE propagator in space. Consider a source region Ω_S and a receiver region Ω_R which are uniformly discretized into N and M grid points, respectively. Define the frequency-dependent kernels:

$$U_1^\omega = [(U_1^\omega)_{i,j}] = \left[\hat{G}_0(\omega, \mathbf{x}_0^i; \mathbf{x}^j) \right]_{1 \leq i \leq N, 1 \leq j \leq M}, \quad (4.32)$$

$$U_2^\omega = [(U_2^\omega)_{i,j}] = \left[\frac{\hat{G}_0(\omega, \mathbf{x}_0^i; \mathbf{x}^j)}{2\tau^2(\mathbf{x}_0^i; \mathbf{x}^j)} \frac{\partial \tau^2(\mathbf{x}_0^i; \mathbf{x}^j)}{\partial x} \right]_{1 \leq i \leq N, 1 \leq j \leq M}, \quad (4.33)$$

$$U_3^\omega = [(U_3^\omega)_{i,j}] = \left[\frac{\hat{G}_0(\omega, \mathbf{x}_0^i; \mathbf{x}^j)}{2\tau^2(\mathbf{x}_0^i; \mathbf{x}^j)} \frac{\partial \tau^2(\mathbf{x}_0^i; \mathbf{x}^j)}{\partial y} \right]_{1 \leq i \leq N, 1 \leq j \leq M}, \quad (4.34)$$

$$U_4^\omega = [(U_4^\omega)_{i,j}] = \left[\frac{\hat{G}_0(\omega, \mathbf{x}_0^i; \mathbf{x}^j)}{2v_0(\mathbf{x}_0^i; \mathbf{x}^j)\tau^2(\mathbf{x}_0^i; \mathbf{x}^j)} \nabla \tau^2(\mathbf{x}_0^i; \mathbf{x}^j) \cdot \nabla v_0(\mathbf{x}_0^i; \mathbf{x}^j) \right]_{1 \leq i \leq N, 1 \leq j \leq M}, \quad (4.35)$$

and the corresponding time-dependent kernels

$$\check{U}_s^t = [(\check{U}_s^t)_{i,j}] = \left[\int_0^{\Delta\omega} e^{i\omega t} U_s^\omega(\mathbf{x}_0^i; \mathbf{x}^j) d\omega \right]_{1 \leq i \leq N, 1 \leq j \leq M}, \quad s = 1, 2, 3, 4. \quad (4.36)$$

We further define vectors

$$\begin{aligned} f_1 &= [\rho(\mathbf{x}^1)u^2(\mathbf{x}^1), \quad \dots, \quad \rho(\mathbf{x}^M)u^2(\mathbf{x}^M)]^T, \\ f_2 &= [c(\mathbf{x}^1)u_x^1(\mathbf{x}^1), \quad \dots, \quad c(\mathbf{x}^M)u_x^1(\mathbf{x}^M)]^T, \\ f_3 &= [c(\mathbf{x}^1)u_y^1(\mathbf{x}^1), \quad \dots, \quad c(\mathbf{x}^M)u_y^1(\mathbf{x}^M)]^T, \\ f_4 &= [\nu(\mathbf{x}^1)u^1(\mathbf{x}^1), \quad \dots, \quad \nu(\mathbf{x}^M)u^1(\mathbf{x}^M)]^T, \\ f_5 &= [\nabla \cdot (\nu(\mathbf{x}^1)\nabla u^1(\mathbf{x}^1)), \quad \dots, \quad \nabla \cdot (\nu(\mathbf{x}^M)\nabla u^1(\mathbf{x}^M))]^T, \\ f_6 &= [c(\mathbf{x}^1)u_x^2(\mathbf{x}^1), \quad \dots, \quad c(\mathbf{x}^M)u_x^2(\mathbf{x}^M)]^T, \\ f_7 &= [c(\mathbf{x}^1)u_y^2(\mathbf{x}^1), \quad \dots, \quad c(\mathbf{x}^M)u_y^2(\mathbf{x}^M)]^T, \\ f_8 &= [\nu(\mathbf{x}^1)u^2(\mathbf{x}^1), \quad \dots, \quad \nu(\mathbf{x}^M)u^2(\mathbf{x}^M)]^T. \end{aligned} \quad (4.37)$$

Then we introduce the following frequency-sampling functions of size $N \times 1$ for $1 \leq k \leq N_\omega$

$$\begin{aligned} \hat{u}_1(\omega_k) &= U_1^{\omega_k} f_1, \\ \hat{u}_2(\omega_k) &= U_2^{\omega_k} f_2 + U_3^{\omega_k} f_3 - U_4^{\omega_k} f_4, \\ \hat{u}_3(\omega_k) &= U_1^{\omega_k} f_5, \\ \hat{u}_4(\omega_k) &= U_2^{\omega_k} f_6 + U_3^{\omega_k} f_7 - U_4^{\omega_k} f_8, \end{aligned} \quad (4.38)$$

and the time-sampling functions of size $N \times 1$ for $0 < t_l \leq \Delta T$

$$\begin{aligned} \check{u}_1(t_\ell) &= \check{U}_1^{t_\ell} f_1, \\ \check{u}_2(t_\ell) &= \check{U}_2^{t_\ell} f_2 + \check{U}_3^{t_\ell} f_3 - \check{U}_4^{t_\ell} f_4, \\ \check{u}_3(t_\ell) &= \check{U}_1^{t_\ell} f_5, \\ \check{u}_4(t_\ell) &= \check{U}_2^{t_\ell} f_6 + \check{U}_3^{t_\ell} f_7 - \check{U}_4^{t_\ell} f_8. \end{aligned} \quad (4.39)$$

Once we obtain all the above sampling functions, according to (3.34) and (3.35), we update $u(t_\ell, \mathbf{x}_0)$ and $u_t(t_\ell, \mathbf{x}_0)$ for all $0 < t_\ell \leq \Delta T$ and $\mathbf{x}_0 \in \Omega_S$ as

$$u(t_\ell, \mathbf{x}_0) \approx \frac{1}{\pi} \Re \left[\check{u}_1(t_\ell) + t_\ell \check{u}_2(t_\ell) + \Delta\omega \sum_{k=1}^{N_\omega-1} e^{-i\omega_k t_\ell} (\hat{u}_1(\omega_k) + t_\ell \hat{u}_2(\omega_k)) \right] \quad (4.40)$$

and

$$u_t(t_\ell, \mathbf{x}_0) \approx \frac{1}{\pi} \Re \left[\check{u}_3(t_\ell) + t_\ell \check{u}_5(t_\ell) + \Delta\omega \sum_{k=1}^{N_\omega-1} e^{-i\omega_k t_\ell} (\hat{u}_3(\omega_k) + t_\ell \hat{u}_4(\omega_k)) \right]. \quad (4.41)$$

4.5 Direct computation of the Hadamard integrators

4.5.1 TFT Eulerian Hadamard integrator

In the following, we present a direct summation algorithm for the TFT Eulerian Hadamard integrator.

Algorithm 1 (TFT Eulerian Hadamard integrator)

1. Uniformly discretize the computational domain Ω into a wave-resolution-satisfying uniform grid; divide Ω into N_I non-overlapping source regions $\{\Omega_S^\ell\}$ and the corresponding receiver regions $\{\Omega_R^\ell\}$, set the large time step $\Delta T < \tau_{\min}$ for updating the initial condition, the small time step $\Delta t = \frac{\Delta T}{N_T}$ for wave resolution, and an ending time T_{end} to ensure that the waves do not reach the computational boundary; determine the bandwidth B according to the initial conditions; set the frequency step $\Delta\omega = \frac{B}{N_\omega}$ where $N_\omega = O(B)$ and generate $\omega_k = (k + \frac{1}{2})\Delta\omega$ for $k = 0, 1, 2, \dots, N_\omega - 1$; pre-compute and compress Hadamard ingredients (4.2) in all sub-region pairs; precompute the diagonal terms for the kernel matrices.
2. Initialize $u(0, \mathbf{x}) = u^1(\mathbf{x})$ and $u_t(0, \mathbf{x}) = u^2(\mathbf{x})$ and set time $T = 0$ and the loop variable $p = 0$.
3. For the current time step with $T = p\Delta T$:
 - (a) compute the finite difference derivatives of $u(T, \mathbf{x})$ and $u_t(T, \mathbf{x})$ and construct the vectors f_1 and f_9 .
 - (b) determine a subregion Ω_p of Ω that contains the region of influence of current data by extending each direction of the non-zero region of $u(T, \mathbf{x})$ outward by $\max c\Delta T$; designate the source regions intersecting with Ω_p as the regions to be updated.
 - (c) for all the source regions Ω_S^ℓ to be updated:
 - i. Interpolate the Hadamard ingredients via partial summation; construct the kernels

$$U_1^{\omega_k}, \quad 0 \leq k \leq N_\omega - 1 \quad \text{and} \quad \check{U}_1^{n\Delta t}, \quad 1 \leq n \leq N_T;$$

compute the matrix-vector multiplications to obtain the frequency- and time- sampling functions

$$\hat{u}_i(\omega_k), \quad i = 1, 5, \quad 0 \leq k \leq N_\omega - 1 \quad \text{and} \quad \check{u}_1(n\Delta t), \quad 1 \leq n \leq N_T.$$

- ii. Update wavefiles $u(T + n\Delta t, \Omega_S^\ell)$ and $u_t(T + n\Delta t, \Omega_S^\ell)$ for $n = 1, 2, \dots, N_T$ via (4.22) and (4.23).
 - (d) Set the wave fields within the source regions that do not require updating to zero.
4. Update $T = (p + 1)\Delta T$. If $T < T_{\text{end}}$, then $p \leftarrow p + 1$ and go to Step 3; else, stop.

Now we consider the computational cost of Algorithm 1. For a given frequency bandwidth B , according to the Shannon sampling theorem, we will have a spatial grid of size $O(B^2)$ in the two-dimensional space. To ensure that wave field is well resolved, we have $\Delta t = O(1/B)$, leading to $O(B^3)$ unknowns to compute.

As mentioned before, $\Delta T = O(1)$ since it only depends on the medium, so as N_I . Thus we will perform Step 3 for $O(1)$ times, and in each iteration, there are $O(B)$ matrix-vector multiplications of size $O(B^2 \times B^2)$, resulting in a computational complexity of at least $O(B^5)$. It is extremely expensive and impractical compared to the number of unknowns. To resolve this issue, we will utilize butterfly algorithms and their hierarchical extensions to accelerate matrix-vector multiplication.

4.5.2 TFTF Eulerian Hadamard integrator

As mentioned earlier, before recursively applying the HKH-TFTF propagator, we shall introduce a smooth approximation of the initial wave field. According to (2.3) and (2.4), we approximate the initial wave fields at time $t \leq \Delta T$ as follows,

$$u(t, \mathbf{x}) \approx G(t, \mathbf{x}_0; \mathbf{x}) \approx \frac{1}{\pi} \Re \left[\int_0^B e^{-i\omega t} \hat{G}_0(\omega, \mathbf{x}_0; \mathbf{x}) d\omega \right], \quad (4.42)$$

and

$$u_t(t, \mathbf{x}) \approx \frac{1}{\pi} \Re \left[\int_0^B (-i\omega) e^{-i\omega t} \hat{G}_0(\omega, \mathbf{x}_0; \mathbf{x}) d\omega \right], \quad (4.43)$$

leading to the truncated, smooth frequency-domain approximations for the wave fields. Although here we have dropped the frequency information beyond the bandwidth B of the time-domain solution, the Shannon sampling theorem indicates that the remaining frequency content is sufficient for reconstructing the band-limited frequency-domain solution with angular frequency $\omega < \frac{B}{2}$ from the truncated wave solution.

In the following we present a direct summation algorithm for the TFTF Eulerian Hadamard integrator.

Algorithm 2 (TFTF Eulerian Hadamard integrator)

1. Uniformly discretize the computational domain Ω into a wave-resolution-satisfying uniform grid; divide Ω into N_I non-overlapping source regions $\{\Omega_S^\ell\}$ and the corresponding receiver regions $\{\Omega_R^\ell\}$, set the large time step $\Delta T < \tau_{\min}$ for updating the initial condition, the small time step $\Delta t = \frac{\Delta T}{N_T}$ for wave resolution, and an ending time T_{end} to ensure that the waves do not reach the computational boundary; determine the bandwidth B according to the angular frequency ω , set the frequency step $\Delta\omega = \frac{B}{N_\omega}$ where $N_\omega = O(B)$ and generate $\omega_k = (k + \frac{1}{2})\Delta\omega$ for $k = 1, 2, \dots, N_\omega - 1$; pre-compute and compress Hadamard ingredients (4.2) in all sub-region pairs; precompute the diagonal terms in kernel matrices.
2. Initialize $u(n\Delta t, \mathbf{x})$ for $n = 1, 2, \dots, N_T$ and $u_t(\Delta T, \mathbf{x})$ using (4.42) and (4.43) and set time $T = \Delta T$ and the loop variable $p = 1$.
3. For the current time step with $T = p\Delta T$:
 - (a) compute the finite difference derivatives of $u(T, \mathbf{x})$ and $u_t(T, \mathbf{x})$ and construct the vectors f_1, f_2, \dots, f_8 .
 - (b) determine a subregion Ω_p of Ω that contains the region of influence of current data by extending each direction of the non-zero region of $u(T, \mathbf{x})$ outward by $\max c\Delta T$; designate the source regions intersecting with Ω_p as the regions to be updated.
 - (c) for all the source regions Ω_S^ℓ to be updated:
 - i. Interpolate the Hadamard ingredients via partial summation; construct the kernels

$$U_s^{\omega_k}, s = 1, 2, 3, 4, 1 \leq k \leq N_\omega - 1, \quad \text{and} \quad \check{U}_s^{n\Delta t}, s = 1, 2, 3, 4, 1 \leq n \leq N_T;$$

compute the matrix-vector multiplications to obtain the corresponding frequency- and time-sampling functions $\{\hat{u}_i(\omega_k)\}$ and $\{\check{u}_i(n\Delta t)\}$:

$$\hat{u}_i(\omega_k), i = 1, 2, 3, 4, 1 \leq k \leq N_\omega - 1, \quad \text{and} \quad \check{u}_i(n\Delta t), i = 1, 2, 3, 4, 1 \leq n \leq N_T.$$
 - ii. Update wavefiles $u(T + n\Delta t, \Omega_S^\ell)$ and $u_t(T + n\Delta t, \Omega_S^\ell)$ for $n = 1, 2, \dots, N_T$ via (4.40) and (4.41).
 - (d) Set the wave fields within the source regions that do not require updating to zero.
4. Update $T = (p + 1)\Delta T$. If $T < T_{\text{end}}$, then $p \leftarrow p + 1$ and go to Step 3; else, go to Step 5.
5. For angular frequency ω , compute the frequency-dependent wavefiled $\hat{u}(\omega, \Omega)$ using (3.36).

Since the number of kernels in the TFTF method is $O(1)$ times that in the TFT method, the computational cost of Step 3 in Algorithm 2 is $O(B^4)$ with a larger prefactor, and fast Fourier transform can be used to reduce the computational cost of the additional Step 5. We can conclude that the computational cost of Algorithm 2 is also $O(B^5)$, and we also obtain $O(B^3)$ unknowns as the time-domain solutions contain information about $O(B)$ frequency-domain solutions with different angular frequencies.

Now we introduce the butterfly algorithms and their hierarchical extensions to accelerate matrix-vector multiplication.

5 Fast computation of Hadamard integrators

Here we propose a butterfly-based algorithm for the construction and application of each kernel, where the complexity and memory usage are reduced from $O(B^4)$ to $O(B^2 \log^2(B))$, leading to the quasi-optimal overall complexity and memory usage.

For large ω_k , the discretized integral operators $U_i^{\omega_k}$ are full rank due to the oscillation of $\hat{G}(\omega_k, \mathbf{x}_0; \mathbf{x})$, but the judiciously selected submatrices of the discretized operators are low-rank compressible due to the so-called complementary low-rank property [27]. Consequently, we can use the butterfly algorithm to compress those frequency-dependent kernels.

Even though the time-dependent kernels do not oscillate (which means that the complementary low-rank property is naturally satisfied), in this work we will use the same butterfly algorithm to compress them. Since the ranks of the submatrices of the time-dependent kernels are smaller than those of the frequency-dependent kernels, this fact naturally help us reduce the computational complexity and memory usage required for compression and application.

The computational region Ω has been divided into N_I source regions $\{\Omega_S^\ell\}$ and corresponding receiver regions $\{\Omega_R^\ell\}$. And we further divide each Ω_R^ℓ into 9 non-overlapping sub-regions where eight of them are adjacent to but not intersecting the source region, and one is coincident with the source region. As shown in Fig. 1, the red square represents the source region Ω_S^ℓ and the overlapping sub-regions, and the eight white squares represent adjacent sub-regions; these subregions together form the receiver region Ω_R^ℓ .

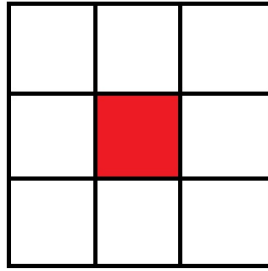


Fig. 1: Illustration of Ω_S^ℓ and Ω_R^ℓ : The red square represents the source region Ω_S , and the largest square divided into nine parts represents the receiver region Ω_R^ℓ

We first describe the interpolative-decomposition butterfly representation for the non-overlapping regions and then introduce the hierarchical structure to handle the overlapping regions.

5.1 Interpolative-decomposition butterfly (IDBF) representation

For the kernel $K(\Omega_1, \Omega_2)$ defined on two non-overlapping regions Ω_1 and Ω_2 , we closely follow [6, 20, 21, 24, 25] to introduce the interpolative-decomposition butterfly algorithm. The algorithm first recursively subdivides the geometrical point sets Ω_1 and Ω_2 associated with the rows and columns of these operators into two subsets of approximately equal sizes using a k-dimensional tree clustering algorithm, until the number of elements in each subset is less than a preset value. When Ω_1 and Ω_2 have different sizes, the number of layers of the binary tree will depend on the smaller one. For the N cell centroids in the computational domain, this procedure generates complete binary trees \mathcal{T}_1 and \mathcal{T}_2 of L levels with root level 0 and leaf level L . Each node τ at level l is an index set $\tau \subset \{1, \dots, N\}$. In both trees, a non-leaf node τ at level l has two children τ_1 and τ_2 , where $\tau = \tau_1 \cup \tau_2$ and $\tau_1 \cap \tau_2 = \emptyset$. For a non-root node τ , its parent is denoted p_τ .

The L -level butterfly representation of the integral operator $K(\Omega_1, \Omega_2) \in \mathbb{C}^{m \times n}$ requires the complementary low-rank property: at any level $0 \leq l \leq L$, for any node τ at level l of \mathcal{T}_1 and any node ν at level $L - l$ of \mathcal{T}_2 , the subblock $K(\tau, \nu)$ is numerically low-rank with rank $r_{\tau, \nu}$ bounded by a small number r called the butterfly rank. As discussed in [24], even if there is a singularity in the integral kernel which

may cause some subblocks to have non-constant ranks, the butterfly algorithm will still work when the singularity only exists at the interface of adjacent regions.

Thus, for any subblock $K(\tau, \nu)$, where $\tau \in \mathcal{T}_1$ and $\nu \in \mathcal{T}_2$, the complementary low-rank property permits a low-rank representation using interpolative decomposition (ID) as

$$K(\tau, \nu) \approx K(\tau, \bar{\nu})V_{\tau, \nu}, \quad (5.1)$$

where the skeleton matrix $K(\tau, \bar{\nu})$ contains $r_{\tau, \nu}$ skeleton columns indexed by $\bar{\nu}$, and the interpolation matrix $V_{\tau, \nu}$ has bounded entries. The ID can be computed via, for instance, rank-revealing QR decomposition with a relative tolerance tol , which actually determines the accuracy of the overall butterfly representation. Here we briefly describe the so-called column-wise butterfly representation [21] [24]

At level $l = 0$, the interpolation matrices $V_{\tau, \nu}$ are explicitly formed, and at level $l > 0$, they are represented in a nested fashion. To see this, consider a node pair (τ, ν) at level $l > 0$ and let ν_1 and ν_2 , and p_τ be the children of ν and parent of τ , respectively. From (5.1), we have

$$\begin{aligned} K(\tau, \nu) &= [K(\tau, \nu_1), K(\tau, \nu_2)] \\ &\approx [K(\tau, \bar{\nu}_1), K(\tau, \bar{\nu}_2)] \begin{bmatrix} V_{p_\tau, \nu_1} & \\ & V_{p_\tau, \nu_2} \end{bmatrix} \\ &\approx K(\tau, \bar{\nu})W_{\tau, \nu} \begin{bmatrix} V_{p_\tau, \nu_1} & \\ & V_{p_\tau, \nu_2} \end{bmatrix}. \end{aligned} \quad (5.2)$$

Here $W_{\tau, \nu}$ and $\bar{\nu}$ are the interpolation matrix and skeleton columns from the ID of $[K(\tau, \bar{\nu}_1), K(\tau, \bar{\nu}_2)]$, respectively. This allows representing $V_{\tau, \nu}$ as

$$V_{\tau, \nu} = W_{\tau, \nu} \begin{bmatrix} V_{p_\tau, \nu_1} & \\ & V_{p_\tau, \nu_2} \end{bmatrix}, \quad (5.3)$$

where we refer $W_{\tau, \nu}$ as the transfer matrix. We will select $O(r_{\tau, \nu})$ proxy rows $\hat{\tau} \subset \tau$ to approximately compute $V_{\tau, \nu}$ and $W_{\tau, \nu}$ via ID:

$$K(\hat{\tau}, \nu) \approx K(\hat{\tau}, \bar{\nu})V_{\tau, \nu}, \quad l = 0, \quad (5.4)$$

$$[K(\hat{\tau}, \bar{\nu}_1), K(\hat{\tau}, \bar{\nu}_2)] \approx K(\hat{\tau}, \bar{\nu})W_{\tau, \nu}, \quad 0 < l < L. \quad (5.5)$$

And we do not select proxy rows at level L .

In this paper, we select the proxy rows as follows. Consider a subblock (τ, ν) at level $0 < l < L$. Let \mathbf{x}^i be the geometrical centroid in the computational domain corresponding to the row index i . Let n_i be the index set consisting of the indices of neighboring centroids of the centroid \mathbf{x}^i , where $i \in \bar{\nu}_1 \cup \bar{\nu}_2$; for example, n_i may be the index set of all indices for centroids that are within a 10 h distance of \mathbf{x}^i . Let f_τ be the index set consisting of $\chi_1 |\bar{\nu}_1 \cup \bar{\nu}_2|$ indices for uniformly selected centroids near the boundary of the subdomain τ with an oversampling parameter χ_1 , and let g_τ denote the index set consisting of $\chi_2 |\bar{\nu}_1 \cup \bar{\nu}_2|$ indices for randomly selected centroids inside the subdomain τ with an oversampling parameter χ_2 . Accordingly, we choose the proxy rows as

$$\hat{\tau} = (\cup_{i \in \bar{\nu}_1 \cup \bar{\nu}_2} n_i) \cap \tau \cup f_\tau \cup g_\tau. \quad (5.6)$$

Numerically, it is sufficient to take the oversampling parameters $\chi_1 = \chi_2 = 3$ for a guaranteed accuracy. The proxy rows can greatly reduce the complexity. With all the interpolation and transfer matrices computed, the butterfly representation of $K(\Omega_1, \Omega_2)$ is:

$$K(\Omega_1, \Omega_2) \approx K^L W^L W^{L-1} \dots W^1 V^0. \quad (5.7)$$

Let ν_1, ν_2, \dots , and $\nu_{2^{L-l}}$ denote the nodes at level $L-l$ of \mathcal{T}_2 , and τ_1, τ_2, \dots , and τ_{2^l} denote the nodes at level l of \mathcal{T}_1 . The interpolation factor V^0 , the transfer factors W^l for $l = 1, \dots, L$, and the skeleton factor K^L are assembled in the following way,

$$V^0 = \text{diag}(V_{\tau, \nu_1}, \dots, V_{\tau, \nu_{2^L}}), \quad (\tau, \nu_i) \text{ at level } l = 0, \quad (5.8)$$

$$K^L = \text{diag}(K(\tau_1, \bar{\nu}), \dots, K(\tau_{2^L}, \bar{\nu})), \quad (\tau_i, \nu) \text{ at level } l = L, \quad (5.9)$$

$$W^l = \text{diag}(W_{\tau_1}, \dots, W_{\tau_{2^{L-l}}}), \quad l = 1, \dots, L, \quad (5.10)$$

$$W_{\tau_i} = \begin{bmatrix} \text{diag}(W_{\tau_i^1, \nu_1}, \dots, W_{\tau_i^1, \nu_{2^{L-l}}}) \\ \text{diag}(W_{\tau_i^2, \nu_1}, \dots, W_{\tau_i^2, \nu_{2^{L-l}}}) \end{bmatrix}, \quad (\tau_i^{\{1,2\}}, \nu_j) \text{ at level } l, \quad (5.11)$$

where τ_i^1 and τ_i^2 denote the children of τ_i .

5.2 Hierarchically off-diagonal butterfly (HODBF) representation

When $\Omega_1 = \Omega_2$, the resulting integral kernels $K(\Omega_1, \Omega_1)$ have singular diagonal terms. We use the hierarchically off-diagonal butterfly (HODBF) [23] [24] representation to resolve such singularities.

We still use the L -level binary tree \mathcal{T}_1 for Ω_1 as in the last subsection. For any two siblings τ_1 and τ_2 with parent τ at level l of \mathcal{T}_1 , we can directly extract two $(L-l)$ -level subtrees \mathcal{T}_{τ_1} and \mathcal{T}_{τ_2} rooted at τ_1 and τ_2 from \mathcal{T}_1 , respectively, due to the nested structure of the binary tree. Next, we construct the $(L-l)$ -level butterfly representation for $K(\tau_1, \tau_2)$ where $\tau_1 \cap \tau_2 = \emptyset$. Finally, there are 2^l butterfly representations at each level $l = 1, 2, \dots, L$. The subblocks $K(\tau, \tau)$ for τ at level L are kept as the dense blocks. Such a representation is called the hierarchically off-diagonal butterfly (HODBF) representation.

5.3 The complexity and memory usage

We analyze the complexity and memory usage of IDBF and HODBF for $K = U_i^\omega$ for $i = 1, 2, 3, 4$ and \check{U}_j^t for $j = 1, 2, 3, 4$. Using the Chebyshev interpolation and partial summation, we can evaluate each element in those kernels with $O(1)$ complexity [24].

For IDBF of $K(\Omega_1, \Omega_2) \in \mathbb{C}^{O(n) \times O(n)}$, we see that, in (5.8)-(5.11), V^0 and K^L contain 2^L diagonal blocks each with $O(r_{\tau,\nu})$ non-zeros, and W^l contains 2^L blocks $W_{\tau,\nu}$ each with $O(r_{\tau,\nu}^2)$ non-zeros. After selecting proxy rows, we will evaluate $O(n)$ IDs of size $O(r_{\tau,\nu}) \times O(r_{\tau,\nu})$ for $O(\log(n))$ levels, resulting in $O(n \log(n))$ complexity and memory usage if $O(r_{\tau,\nu}) = O(1)$, analogous to the classic result of the butterfly algorithm.

However, for the kernel with singularity near the interface in our setting, we follow [24] to analyze the sub-blocks near the interface separately. Let $l_m = \frac{L}{2}$ denote the middle butterfly level; there are $O(N)$ subblocks $K(\tau, \nu)$ at each level l , and there are $O(2^{l-l_m/2} n^{1/4})$ subblocks representing interactions between adjacent or close-by geometric subdomains. The non-constant ranks of these subblocks scale as $r_{\tau,\nu} = O(2^{-|l-l_m|/2} n^{1/4})$, which are dominated by the interface degree-of-freedom (DOFs) between the two subdomains. Moreover, each non-constant-rank subblock requires $O(r_{\tau,\nu}^2)$ memory usage and matrix entry computation and $O(r_{\tau,\nu}^3)$ ID cost. Thus, they require

$$\sum_l r_{\tau,\nu}^2 O(2^{|l-l_m|/2} n^{1/4}) = O(n^{3/4}) \leq O(n) \quad \text{memory usage} \quad (5.12)$$

and

$$\sum_l r_{\tau,\nu}^3 O(2^{|l-l_m|/2} n^{1/4}) = O(n) \quad \text{complexity} . \quad (5.13)$$

Hence, we can still state that the memory usage and complexity of the IDBF for $K \in \mathbb{C}^{O(n) \times O(n)}$ are $O(n \log(n))$. Due to the $O(n \log(n))$ nonzeros, we immediately conclude that the complexity of application of the IDBF matrix is $O(n \log(n))$.

For HODBF of $K(\Omega_1, \Omega_1) \in \mathbb{C}^{O(N) \times O(N)}$, letting $L = O(\log(N))$ denote the level of the binary tree \mathcal{T}_1 , we follow the DOFs analysis in [31] to sum up the complexity and memory usage of the $L-l$ -level butterfly for all level l and the 2^L dense blocks at level L ,

$$2^L O(1) + \sum_{l=1}^L 2^l O(N/2^l \log(N/2^l)) = O(N \log^2(N)). \quad (5.14)$$

That is, the the memory usage and complexity of the construction and application of the HODBF for $K(\Omega_1, \Omega_1) \in \mathbb{C}^{O(N) \times O(N)}$ are $O(N \log^2(N))$.

5.4 Butterfly-compressed TFT Eulerian Hadamard integrators

Starting from Algorithm 1, with the help of IDBF and HODBF, we precompute the low-rank representations of frequency-dependent kernels $U_1^{\omega_k}$ and corresponding time-dependent kernels \check{U}_1^ℓ and apply those compressed kernels in each time step, resulting in the butterfly-compressed TFT Hadamard integrator (Algorithm 3) with quasi-linear memory usage and computational complexity.

Algorithm 3: Butterfly-compressed TFT Eulerian Hadamard integrator

1. Uniformly discretize the computational domain Ω into a wave-resolution-satisfying uniform grid; divide Ω into N_I non-overlapping source regions $\{\Omega_S^\ell\}$ and the corresponding receiver regions $\{\Omega_R^\ell\}$, set the large time step $\Delta T < \tau_{\min}$ for update the initial condition, the small time step $\Delta t = \frac{\Delta T}{N_T}$ for wave resolution and an ending time T_{end} to ensure that the waves do not reach the computational boundary; determine the bandwidth B according to the initial conditions, set the frequency step $\Delta\omega = \frac{B}{N_\omega}$ where $N_\omega = O(B)$ and generate $\omega_k = (k + \frac{1}{2})\Delta\omega$ for $k = 0, 1, 2, \dots, N_\omega - 1$; pre compute and compress Hadamard ingredients (4.2) in all subregions pairs.
2. For each source region Ω_S^ℓ , divide the corresponding receiver region Ω_R^ℓ into several subregions that are similar in size to the source region, including a subregion that coincides with the source region and several adjacent subregions; compute the IDBF and HODBF representations of

$$U_1^{\omega_k}, 0 \leq k \leq N_\omega - 1 \quad \text{and} \quad \tilde{U}_1^{n\Delta t}, 1 \leq n \leq N_T.$$

3. Initialize $u(0, \mathbf{x}) = u^1(\mathbf{x})$, $u_t(0, \mathbf{x}) = u^2(\mathbf{x})$ and set time $T = 0$ and loop variable $p = 0$.
4. For the current time step with $T = p\Delta T$:
 - (a) compute the numerical differentiations of $u(T, \mathbf{x})$ and $u_t(T, \mathbf{x})$ and construct the vectors f_1 and f_9 .
 - (b) determine a subregion Ω_p of Ω that contains the region of influence of current data by extending each direction of the non-zero region of the $u(T, \mathbf{x})$ outward by $\max c\Delta T$; designate the source regions intersecting with Ω_p as the regions to be updated.
 - (c) for all the source regions Ω_S^ℓ to be update:
 - i. apply the IDBF matrices and HODBF matrices to obtain the corresponding frequency- and time- sampling functions

$$\hat{u}_i(\omega_k), i = 1, 5, 0 \leq k \leq N_\omega - 1 \quad \text{and} \quad \hat{u}_1(n\Delta t), 1 \leq n \leq N_T.$$

- ii. update wavefiles $u(T + n\Delta t, \Omega_S^\ell)$ and $u_t(T + n\Delta t, \Omega_S^\ell)$ via (4.22) and (4.23).
 - (d) set the wave fields within the source regions that do not require updating to zero.
5. Update $T = (p + 1)\Delta T$. If $T < T_{\text{end}}$, then $p \leftarrow p + 1$ and go to Step 3; else, stop.

Equipped with butterfly decomposition, we construct the frequency-domain and time-domain kernels in the precomputation step and recursively apply them during time marching. The computational complexity and memory usage of constructing and applying each kernel are reduced from $O(B^4)$ to $O(B^2 \log^2(B))$, resulting in the Eulerian Hadamard integrator with overall complexity and memory usage of $O(B^3 \log^2(B))$. Although we divide Ω into N_I parts, $N_I = O(1)$ which only depends on the medium; consequently, such partition does not affect the overall complexity estimate.

Further, assume that we solve the wave equation with m_1 different initial conditions simultaneously. In this case, we only construct the $O(B)$ kernels once, and the computational cost is

$$O(B)O(B^2 \log^2(B)) \doteq O(C_1 B^3 \log^2(B));$$

we further apply all those kernels to m_1 initial conditions, and the computational cost is $O(m_1 C_2 B^3 \log^2(B))$; we use the fast Fourier transform to obtain the time-domain solutions on $O(B_m^3)$ mesh points, and the cost is $O(m_1 B_m^3 \log(B))$. Since we only need to update the initial conditions for $\frac{T_{\text{end}}}{\Delta T} = O(1)$ times, the overall computational complexity is

$$O\left((C_1 + \frac{T_{\text{end}}}{\Delta T} m_1 C_2) B^3 \log^2(B)\right).$$

For the butterfly algorithm, C_1 depends on the accuracy of the representation and depends on $r_{\tau, \nu}^3$ from the IDs. In any case, C_1 is far greater than C_2 ; thus, when solving different Cauchy problems in the same medium, the efficiency of the algorithm will be more significant. On the other hand, even if IDBF and HODBF need to be recalculated at each step due to limited computing resources, the overall computational complexity is still quasi-linear.

The quasi-linear memory usage makes parallel computing applicable. Since there are $O(B)$ kernels to compress, we do not embed parallel computing into the decomposition of each kernel matrix, and, instead, we use the parallel toolbox in Matlab to simultaneously calculate the butterfly decomposition of $O(B)$ kernel matrices.

5.5 Butterfly-compressed TFTF Eulerian Hadamard integrators

Starting from Algorithm 2, with the help of IDBF and HODBF, we precompute the low-rank representations of frequency-dependent kernels $U_i^{\omega_k}$ for $i = 1, 2, 3, 4$ and corresponding time-dependent kernels \tilde{U}_j^ℓ for $j = 1, 2, 3, 4$ and apply those compressed kernels in each time step, resulting in the butterfly-compressed TFTF Hadamard integrator (Algorithm 4) with quasi-linear memory usage and computational complexity.

Algorithm 4: Butterfly-compressed TFTF Eulerian Hadamard integrator

1. Uniformly discretize the computational domain Ω into a wave-resolution-satisfying uniform grid; divide Ω into N_I non-overlapping source regions $\{\Omega_S^\ell\}$ and the corresponding receiver regions $\{\Omega_R^\ell\}$, set the large time step $\Delta T < \tau_{\min}$ for update the initial condition, the small time step $\Delta t = \frac{\Delta T}{N_T}$ for wave resolution and an ending time T_{end} to ensure that the waves do not reach the computational boundary; determine the bandwidth B according to the angular frequency, set the frequency step $\Delta\omega = \frac{B}{N_\omega}$ where $N_\omega = O(B)$ and generate $\omega_k = (k + \frac{1}{2})\Delta\omega$ for $k = 0, 1, 2, \dots, N_\omega - 1$; pre compute and compress Hadamard ingredients (4.2) in all sub-regions pairs.
2. For each source region Ω_S^ℓ , divide the corresponding receiver region Ω_R^ℓ into several subregions that are similar in size to the source region, including a subregion that coincides with the source region and several adjacent subregions; compute the IDBF and HODBF representations of

$$U_s^{\omega_k}, s = 1, 2, 3, 4, 1 \leq k \leq N_\omega - 1 \quad \text{and} \quad \tilde{U}_s^{n\Delta t}, s = 1, 2, 3, 4, 1 \leq n \leq N_T.$$

3. Initialize $u(n\Delta t, \mathbf{x})$, $n = 1, 2, \dots, N_T$ and $u_t(\Delta T, \mathbf{x})$ using (4.42) and (4.43), set time $T = \Delta T$ and loop variable $p = 1$.
4. For the current time step with $T = p\Delta T$:
 - (a) compute the numerical differentiations of $u(T, \mathbf{x})$ and $u_t(T, \mathbf{x})$ and construct the vectors f_1, f_2, \dots, f_8 .
 - (b) determine a subregion Ω_p of Ω that contains the region of influence of current data by extending each direction of the non-zero region of the $u(T, \mathbf{x})$ outward by $\max c\Delta T$; designate the source regions intersecting with Ω_p as the regions to be updated.
 - (c) for all the source regions Ω_S^ℓ to be update:
 - i. apply the IDBF matrices and HODBF matrices to obtain the corresponding frequency- and time- sampling functions

$$\hat{u}_i(\omega_k), i = 1, 2, 3, 4, 1 \leq k \leq N_\omega - 1, \quad \text{and} \quad \tilde{u}_i(n\Delta t), i = 1, 2, 3, 4, 1 \leq n \leq N_T.$$

ii. update wavefields $u(T + n\Delta t, \Omega_S^\ell)$ and $u_t(T + n\Delta t, \Omega_S^\ell)$ via (4.40) and (4.41).

(d) set the wave fields within the source regions that do not require updating to zero.

5. Update $T = (p + 1)\Delta T$. If $T < T_{\text{end}}$, then $p \leftarrow p + 1$ and go to Step 3; else, go to Step 5.

6. for angular frequency ω , compute the frequency-dependent wavefield $\hat{u}(\omega, \Omega)$ using (3.36).

We can carry out the complexity analysis similar to the one in Section 5.4. The difference in the computational complexity between the TFT method and the TFTF method comes from that in the number of kernels, and the overall computational complexity and memory usage are also $O(B^3 \log^2(B))$. Since the kernels in the TFTF method include the kernels of the TFT method, this helps us reduce the computational cost of the precomputation.

6 Numerical examples

This section provides several numerical examples to demonstrate the accuracy and efficiency of the proposed butterfly-compressed Hadamard integrators by solving wave equations in time and frequency domain. All computations were performed on a computer equipped with 512GB of RAM and two 28-core Intel Xeon 6258R processors.

Because exact solutions for the wave equations are not available in general, we numerically solve the wave equation with a finite-difference pseudo-spectral method for time-domain solutions and a finite-difference based direct solver for frequency-domain solutions, where we always keep the number of points per wavelength (PPW) larger than 40 to reduce the dispersion error. For the proposed Hadamard integrator, we will set $\text{PPW} \sim 5$ with respect to the artificial bandwidth B .

6.1 Sinusoidal model

We introduce a sinusoidal model with the following setup.

- $\rho = \frac{1}{(1 + 0.2 \sin(3\pi(x + 0.05)) \sin(0.5\pi y))^2}$, $\nu = 1$ such that $c = 1 + 0.2 \sin(3\pi(x + 0.05)) \sin(0.5\pi y)$.
- $B = 64\pi$, $h = \frac{1}{192}$, $\Delta\omega = \frac{\pi}{2}$, and $\Delta t = \frac{1}{192}$.
- $\Omega = [-1, 2] \times [-1, 2]$; the sizes of Ω_S^ℓ and Ω_R^ℓ are 0.2×0.2 and 0.6×0.6 respectively; $\Delta T = \frac{1}{8}$.
- Orders of Chebyshev interpolation of Hadamard ingredients in the four variables x_0 , y_0 , x , and y are 11, 11, 13, and 13, respectively.
- Tolerance used in interpolative decomposition $\text{tol} = 1e - 9$.

6.1.1 TFT method for Case 1

For Case 1, we take the initial conditions as

$$u(0, x, y) = \sin(\beta\pi \frac{x+y-1}{\sqrt{2}}) \exp(-100((x-0.5)^2 + (y-0.5)^2)), \quad u_t(0, x, y) = 0, \quad (6.1)$$

where $\beta = 8, 16$ and 32 , respectively, and we utilize the Hadamard integrator to simultaneously solve these three Cauchy problems. Fig. 2 shows the comparisons between the TFT solutions and the exact solutions in $[0, 1] \times [0, 1]$ with $t = 0.5$. In Fig. 3, we further compare the solutions along some lines.

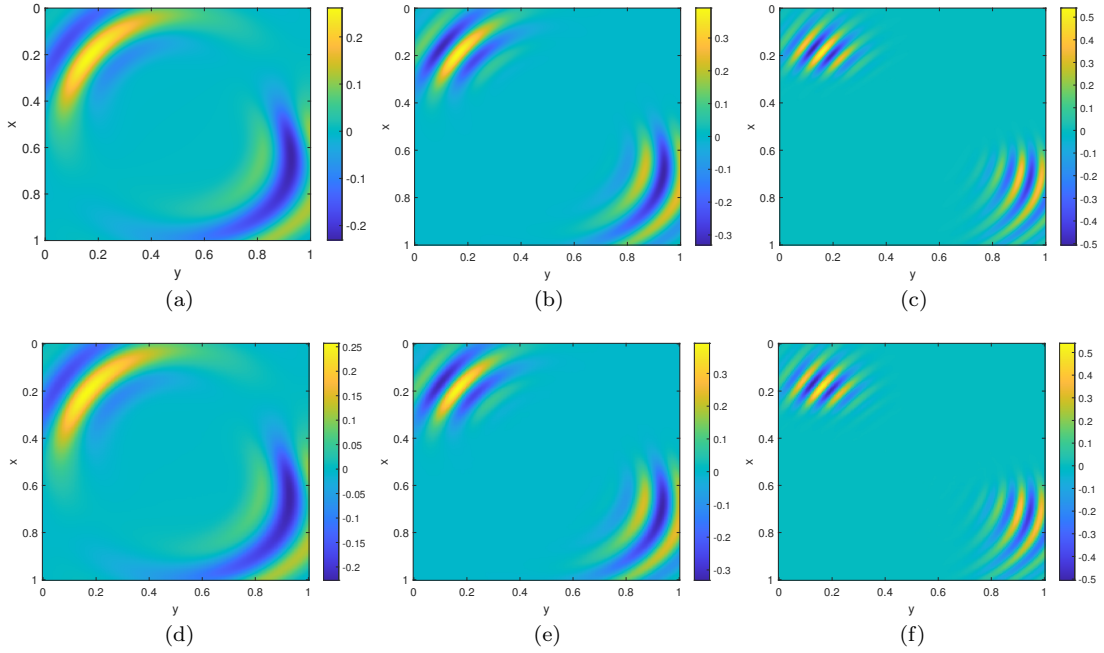


Fig. 2: Sinusoidal model. $u(t, \mathbf{x})$, $t = 0.5$: (a) TFT solution with $\beta = 8$; (b) TFT solution with $\beta = 16$; (c) TFT solution with $\beta = 32$; (d) exact solution with $\beta = 8$; (e) exact solution with $\beta = 16$; (f) exact solution with $\beta = 32$

6.1.2 TFTF method for Case 2

For Case 2, taking $\mathbf{z} = [0.5, 0.5]$ and $T_{\text{end}} = 1.5$, we obtain the time-domain point-source wave fields $u(t, \mathbf{x})$. As shown in Fig. 4, we can clearly observe the occurrence of caustics.

Further applying the Fourier transform, we obtain the frequency-domain point-source wave fields $\hat{u}(\omega, \mathbf{x})$ with different angular frequencies ω . In Fig. 5, we compare the TFTF solution with the exact solution for $\omega = 8\pi, 16\pi$ and 32π , and $\mathbf{x} \in [0, 1.5] \times [0, 1.5]$.

Fig. 6 shows the comparisons of the two solutions along some lines that traverse through the caustics region for various ω . Although they match well, it can be observed that the errors at $\omega = 8\pi$ and 32π are slightly larger than those at $\omega = 16\pi$, and we will explain this phenomenon in Section 6.4.

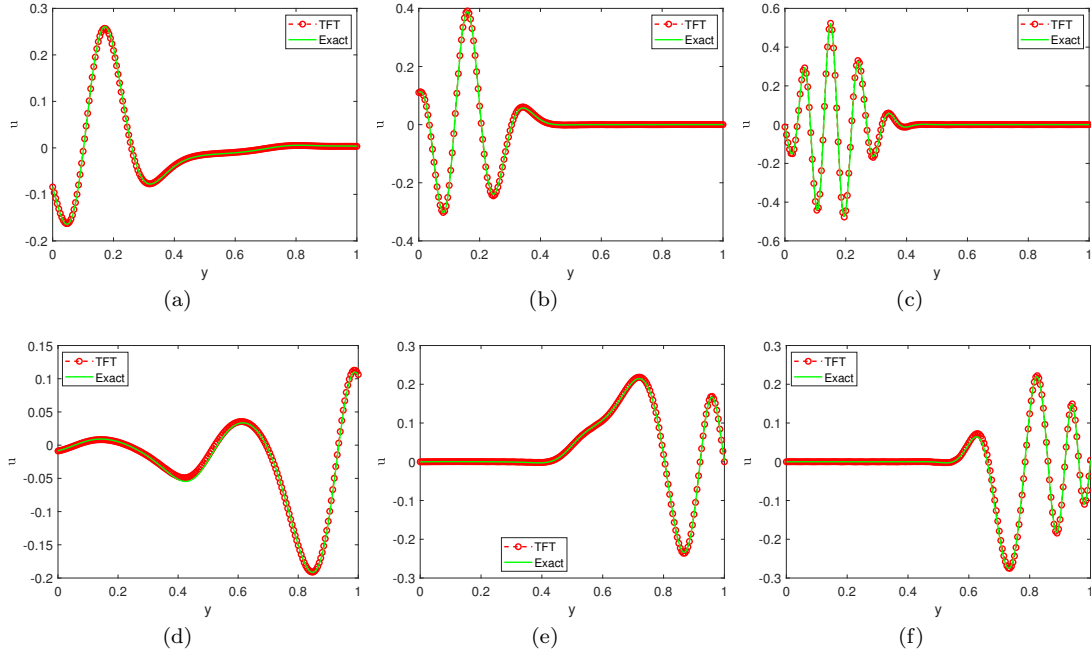


Fig. 3: Sinusoidal model. Slices of time-domain wave fields $u(t, \mathbf{x})$ when $t = 0.5$: (a) a slice at $x = 0.2$ with $\beta = 8$; (b) a slice at $x = 0.2$ with $\beta = 16$; (c) a slice at $x = 0.2$ with $\beta = 24$; (d) a slice at $y = 0.85$ with $\beta = 8$; (e) a slice at $y = 0.85$ with $\beta = 16$; (f) a slice at $y = 0.85$ with $\beta = 24$

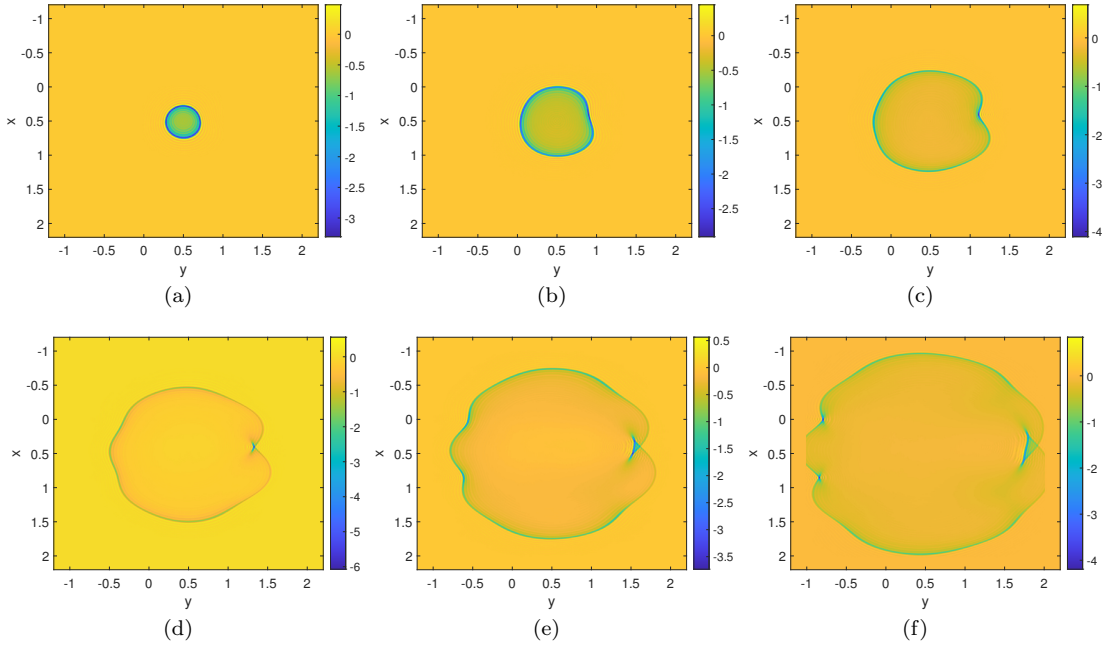


Fig. 4: Sinusoidal model. Time-domain point source wave fields $u(t, \mathbf{x})$. (a): $T = 0.25$; (b): $T = 0.5$; (c): $T = 0.75$; (d): $T = 1$; (e): $T = 1.25$; (f): $T = 1.5$

6.2 Smoothed Heaviside model

We introduce a y -dependent velocity model c , which is analogous to a scaled, smoothed, and shifted Heaviside function.

- $\rho = \left(\frac{1 + e^{-20(y-1)}}{1.25 + 0.8e^{-20(y-1)}} \right)^2$ and $\nu = 1$ such that $c = 0.8 + \frac{0.45}{1 + e^{-20(y-1)}}$.
- $B = 48\pi$, $h = \frac{1}{160}$, $\Delta\omega = \frac{\pi}{2}$, and $\Delta t = \frac{1}{144}$.
- $\Omega = [-3, 3] \times [-1, 4]$; the sizes of Ω_S^ℓ and Ω_R^ℓ are 0.2×0.2 and 0.6×0.6 respectively; $\Delta T = \frac{1}{8}$.

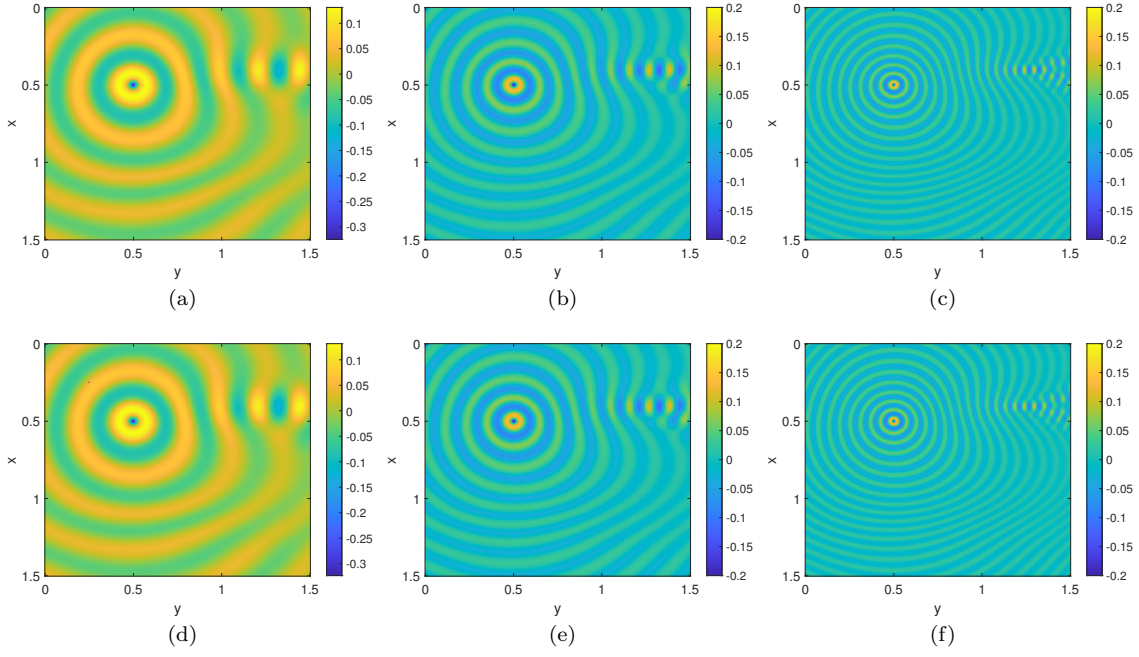


Fig. 5: Sinusoidal model. $\hat{u}(\omega, \mathbf{x})$. (a): TFTF solution with $\omega = 8\pi$; (b): TFTF solution with $\omega = 16\pi$; (c): TFTF solution with $\omega = 32\pi$; (d): exact solution with $\omega = 8\pi$; (e): exact solution with $\omega = 16\pi$; (f): exact solution with $\omega = 32\pi$

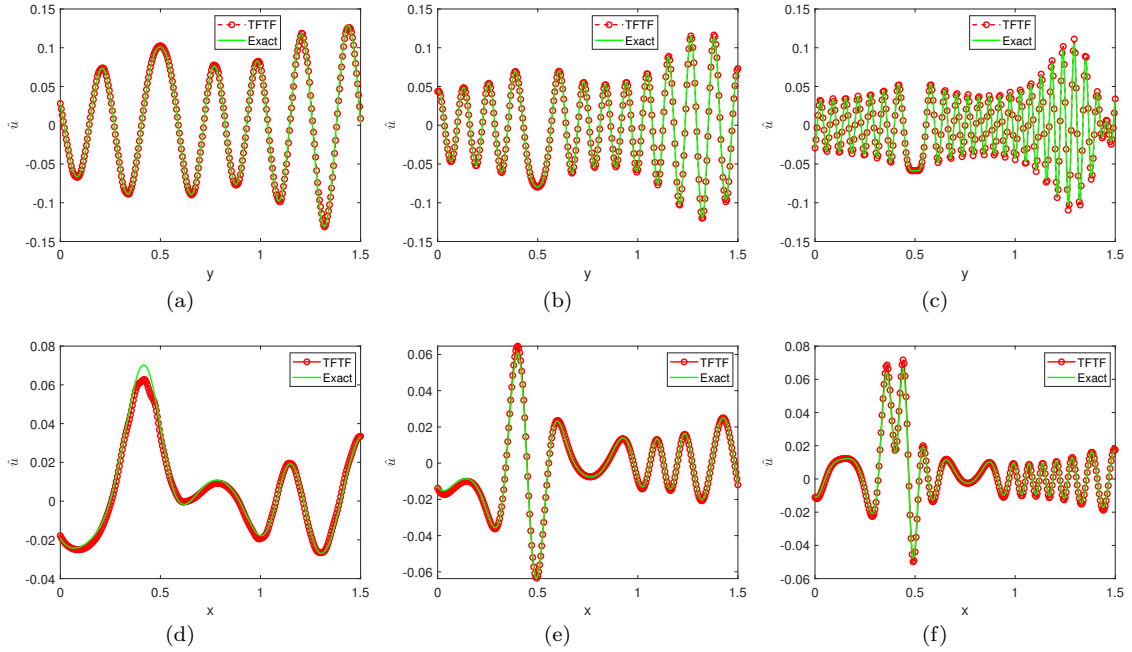


Fig. 6: Sinusoidal model. Slices of frequency-domain point source wave fields $\hat{u}(\omega, \mathbf{x})$. (a) a slice at $x = 0.4$ with $\omega = 8\pi$; (b) a slice at $x = 0.4$ with $\omega = 16\pi$; (c) a slice at $x = 0.4$ with $\omega = 32\pi$; (d) a slice at $y = 1.4$ with $\omega = 8\pi$; (e) a slice at $y = 1.4$ with $\omega = 16\pi$; (f) a slice at $y = 1.4$ with $\omega = 32\pi$

- Orders of Chebyshev interpolation of Hadamard ingredients in the four variables x_0 , y_0 , x , and y are 11, 11, 13, and 13, respectively.
- Tolerance used in interpolative decomposition $\text{tol} = 1e - 9$.

6.2.1 TFT method for Case 1

For Case 1, we take the initial conditions as

$$u(0, x, y) = \sin(\beta\pi \frac{x+y-1}{\sqrt{2}}) \exp(-100(x^2 + (y-0.8)^2)), \quad u_t(0, x, y) = 0, \quad (6.2)$$

where $\beta = 8, 16, 24$, respectively, and we utilize the Hadamard integrator to simultaneously solve these three Cauchy problems. Fig. 7 shows the comparisons between the TFT solutions and the exact solutions with $t = 0.5$. Fig. 8 further compare the solutions along some lines.

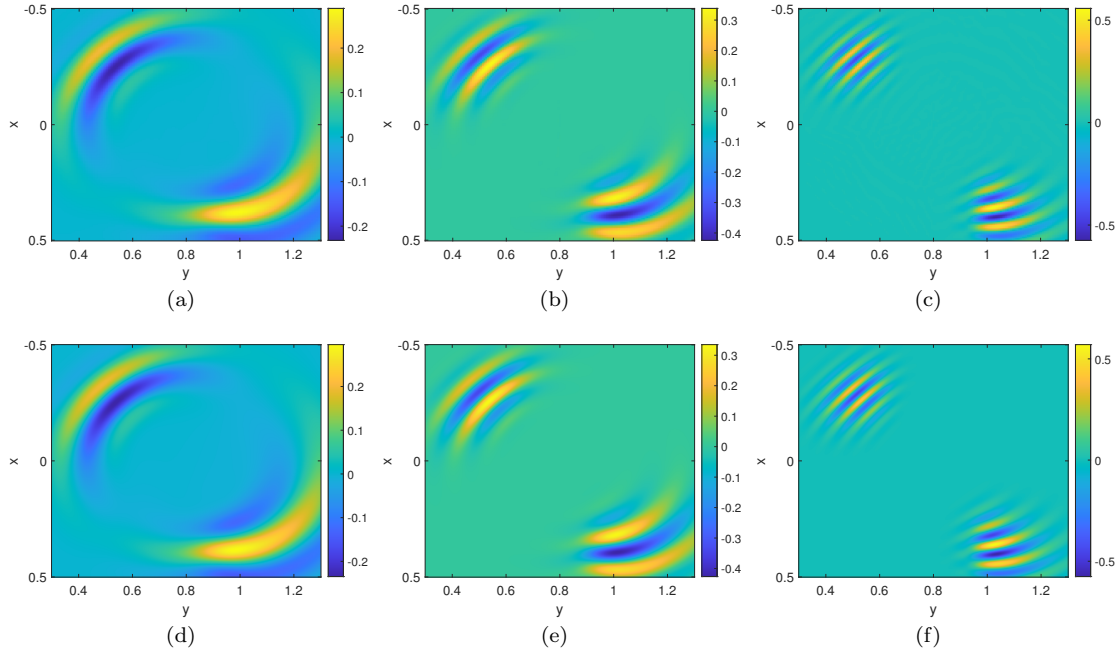


Fig. 7: Heaviside model. $u(t, \mathbf{x})$, $t = 0.5$: (a) TFT solution with $\beta = 8$; (b) TFT solution with $\beta = 16$; (c) TFT solution with $\beta = 32$; (d) exact solution with $\beta = 8$; (e) exact solution with $\beta = 16$; (f) exact solution with $\beta = 32$

6.2.2 TFTF method for Case 2

For Case 2, taking $\mathbf{z} = [1, 0.8]$ and $T_{end} = 2$, we obtain the time-domain point-source wave fields $u(t, \mathbf{x})$. As shown in Fig. 9, we can clearly observe the caustics induced by the overturning rays.

Further applying the Fourier transform, we obtain the frequency-domain point source wave fields $\hat{u}(\omega, \mathbf{x})$ with different angular frequencies ω . In Fig. 10, we compare the TFTF solution with the exact solution for $\omega = 8\pi, 16\pi$, and 24π , and $\mathbf{x} \in [-0.6, 1.4] \times [0.5, 2.5]$.

Fig. 11 shows the comparisons of the two solutions along some lines that traverse through the caustics region for various frequencies ω . The TFTF solutions match exact solutions well.

6.3 Complexity validation

In this subsection, we validate the CPU and memory complexities of the proposed Eulerian Hadamard integrator. Here we use the Sinusoidal model, and we set the source region $\Omega_1 = [-0.1, 0.1] \times [-0.1, 0.1]$ and one of the corresponding adjacent receiver subregions $\Omega_2 = [-0.3, 0.1] \times [-0.1, 0.1]$.

Since there exist singularities in our kernels, the compression error will increase as the grid becomes finer; however, we can choose proper tolerance tol and oversampling parameters χ_1 and χ_2 so that even for extremely fine meshes ($h = \frac{1}{3200}$), the maximum relative error is controlled to be smaller than $1e-4$, which can be neglected in comparison to other errors. We can state that for given tol , χ_1 and χ_2 , the

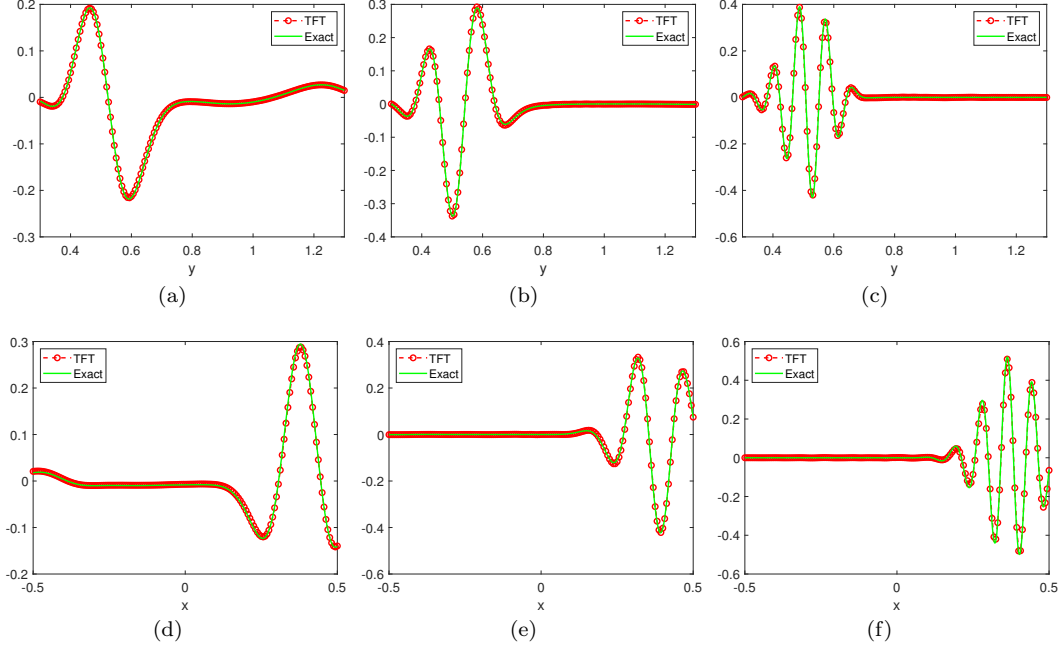


Fig. 8: Heaviside model. Slices of time-domain wave fields $u(t, \mathbf{x})$ when $t = 0.5$: (a) a slice at $x = -0.3$ with $\beta = 8$; (b) a slice at $x = -0.3$ with $\beta = 16$; (c) a slice at $x = -0.3$ with $\beta = 24$; (d) a slice at $y = 1$ with $\beta = 8$; (e) a slice at $y = 1$ with $\beta = 16$; (f) a slice at $y = 1$ with $\beta = 24$

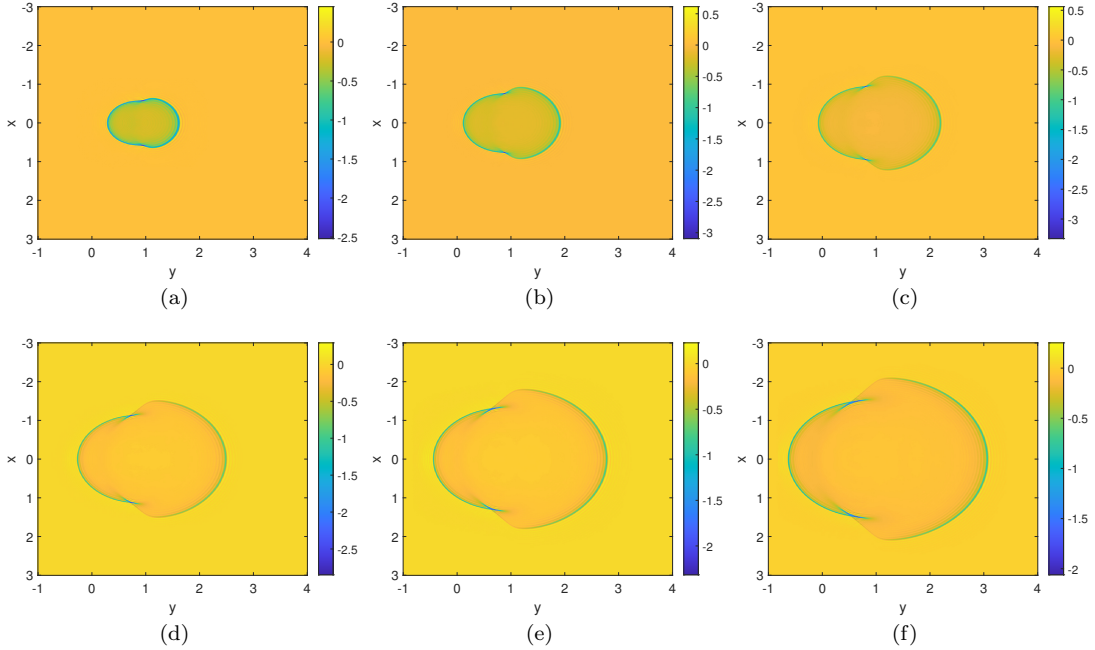


Fig. 9: Heaviside model. Time-domain point source wave fields $u(t, \mathbf{x})$. (a): $T = 0.75$; (b): $T = 1$; (c): $T = 1.25$; (d): $T = 1.5$; (e): $T = 1.75$; (f): $T = 2$

computational complexity and the CPU memory usage of the butterfly compression grow as $O(N \log(N))$ for IDBF and $O(N \log^2(N))$ for HODBF, respectively.

We set $tol = 1e - 9$ and $\chi_1 = \chi_2 = 3$, and we vary the frequency and cell count from $\omega = 10\pi$ and $N = 81^2$ to $\omega = 160\pi$ and $N = 1281^2$, respectively. We sequentially construct the IDBF matrices of the kernels $U_1^\omega(\Omega_1, \Omega_2)$, $U_2^\omega(\Omega_1, \Omega_2)$, $U_3^\omega(\Omega_1, \Omega_2)$ and $U_4^\omega(\Omega_1, \Omega_2)$ and HODBF matrices of the kernels $U_1^\omega(\Omega_1, \Omega_1)$, $U_2^\omega(\Omega_1, \Omega_1)$, $U_3^\omega(\Omega_1, \Omega_1)$ and $U_4^\omega(\Omega_1, \Omega_1)$. And we record the total CPU time and total

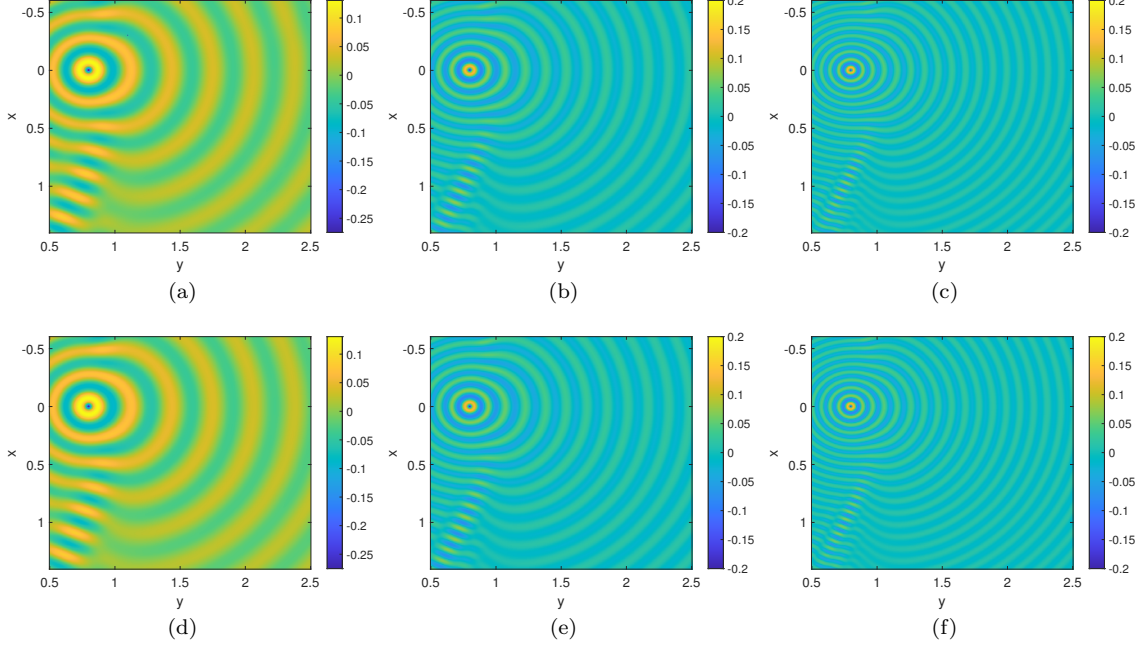


Fig. 10: Heaviside model. $\hat{u}(\omega, \mathbf{x})$. (a): TFTF solution with $\omega = 8\pi$; (b): TFTF solution with $\omega = 16\pi$; (c): TFTF solution with $\omega = 24\pi$; (d): exact solution with $\omega = 8\pi$; (e): exact solution with $\omega = 16\pi$; (f): exact solution with $\omega = 24\pi$

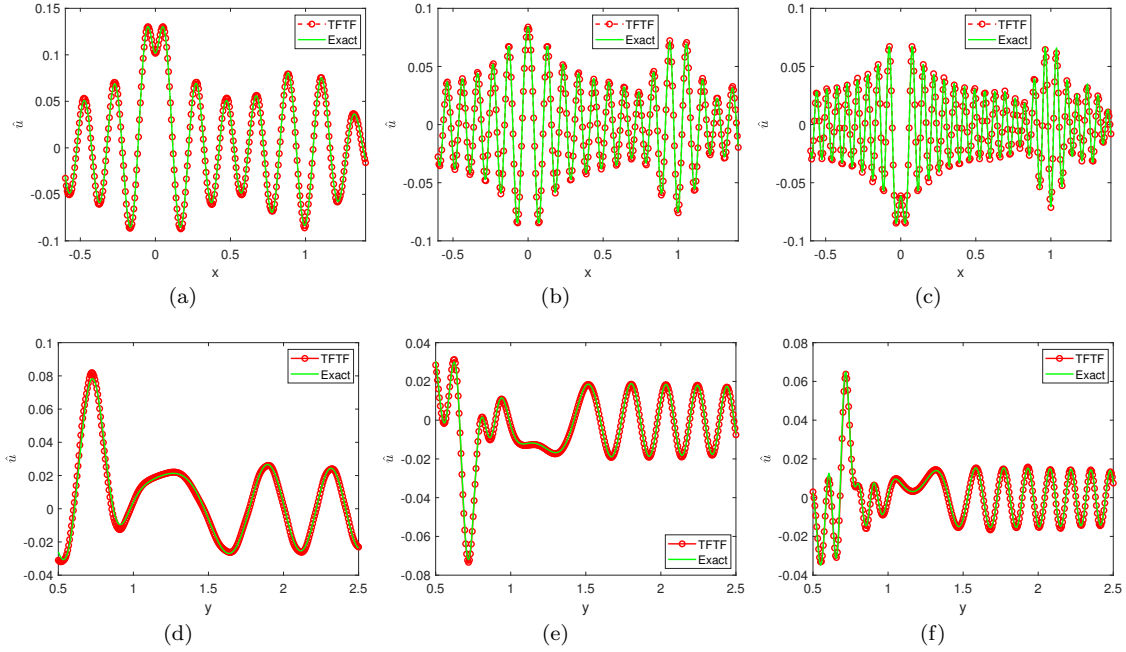


Fig. 11: Heaviside model. Slices of frequency-domain point source wave fields $\hat{u}(\omega, \mathbf{x})$. (a): a slice at $y = 0.75$ with $\omega = 8\pi$; (b): a slice at $y = 0.75$ with $\omega = 16\pi$; (c): a slice at $y = 0.75$ with $\omega = 24\pi$; (d): a slice at $x = 1.3$ with $\omega = 8\pi$; (e): a slice at $x = 1.3$ with $\omega = 16\pi$; (f): a slice at $x = 1.3$ with $\omega = 24\pi$

memory usage of IDBF and HODBF respectively. The CPU time and memory usage for constructing the IDBF and HODBF matrices are plotted in Fig. 12 and Fig. 13, which validate our complexity estimates.

Due to its quasi-linear memory usage, the computations of IDBF and HODBF can be parallelized quite directly. Although there are $O(B)$ kernels to compress, we will not embed parallelism into the algorithm so that we will only show the computational time of a sequential implementation of the algorithm. Nevertheless, simply using ‘parfor’ with respect to ω_k and t_ℓ reduces the computational time of each kernel by roughly $O(N_c)$ times, where N_c is the number of cores of the computer, and parallel implementation

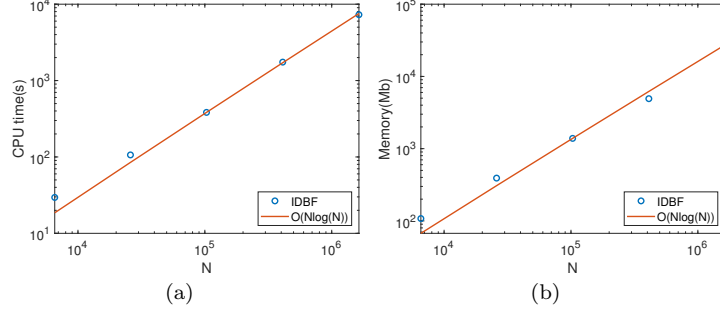


Fig. 12: CPU time and memory usage of IDBF without parallel implementation

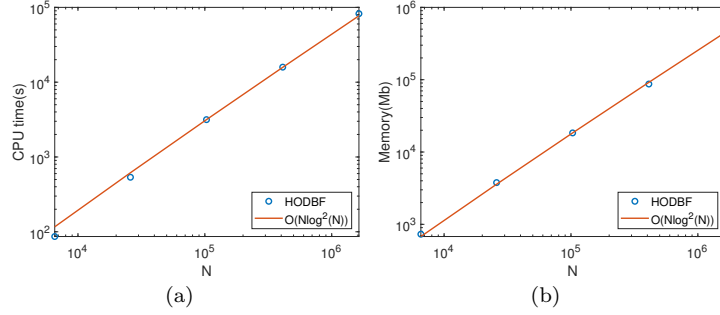


Fig. 13: CPU time and memory usage of HODBF without parallel implementation

on the 56-core computer that we used here can improve the efficiency of the IDBF and HODBF in our numerical examples by roughly about 25 times.

6.4 Convergence test

As mentioned earlier, B is an artificial frequency bandwidth, and ω or β is the frequency parameter from the problem, both of which affect the accuracy of the Hadamard integrator.

In the TFT method for Case 1, we have assumed that the time-domain solution $u(t, \mathbf{x})$ decays rapidly in the frequency domain, which means that increasing B will not improve the accuracy of the TFT solution. On the other hand, we regard β as a frequency parameter, but as $\beta \rightarrow 0$, the frequency-domain bandwidth of the solution does not tend to zero, due to the influence of components in the initial conditions that ensure compact support. Consequently, it is non-trivial to discuss the asymptotic behavior of the TFT method in terms of B or β , and thus we will not do that here. However, we need to choose an appropriately large B in conjunction with β to ensure the rapid decay beyond the bandwidth.

In the TFTF method for Case 2, generating the time-domain Green's function from the Fourier summation of frequency-domain Green's functions yields an $O(\frac{1}{B^{0.5}})$ asymptotic error according to (4.24). However, when using these time-domain solutions to generate the final frequency-domain solution, we observe an asymptotic behavior of $O(\frac{1}{B})$, which we believe is due to the fact that the TFTF method is somewhat analogous to reconstructing a signal using the Fourier transform. On the other hand, the angular frequency also affects the accuracy. According to [24], taking the one-term Babich's ansatz $\hat{G}_0(\omega, \mathbf{x}_0; \mathbf{x})$ as the frequency-domain Green's function introduces an $O(\frac{1}{\omega^{1.5}})$ asymptotic error.

To verify the asymptotic behavior with respect to ω , we take the angular frequency $\omega = 2\pi, 4\pi, 8\pi$, and 16π , respectively, and evaluate the L^2 -error with respect to the exact solution. As shown in Fig. 14(a), when ω is small, the asymptotic error of the one-term Babich's ansatz dominates so that we can obtain $O(\frac{1}{\omega^{1.5}})$ convergence.

To verify the asymptotic behavior with respect to B , we consider the following setups in the Sinusoidal model:

1. $B = 32\pi$, $h = \frac{1}{100}$, and $\Delta t = \frac{1}{96}$;
2. $B = 48\pi$, $h = \frac{1}{160}$, and $\Delta t = \frac{1}{144}$;
3. $B = 64\pi$, $h = \frac{1}{200}$, and $\Delta t = \frac{1}{192}$.

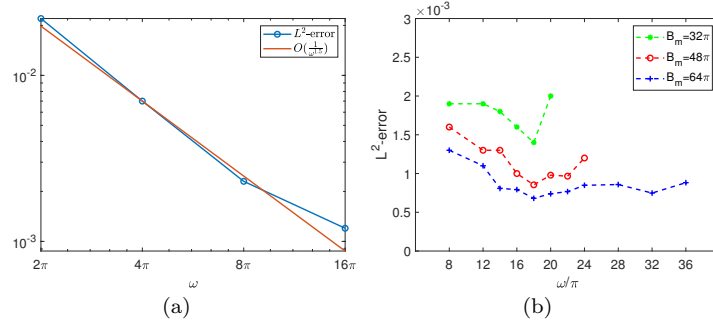


Fig. 14: Convergence. (a): L^2 -error with $B = 64\pi$ and different ω ; (b): L^2 -error with different B and ω

We further set $T_{end} = 1$ and compute the frequency-domain solution in $[0.2, 1.2] \times [0.2, 1.2]$. The L^2 errors for different B and ω are shown in Fig. 14(b).

For a fixed B , as ω increases, the error decreases initially due to the dominance of the asymptotic error from Babich's ansatz. Subsequently, the error saturates due to the dominance of the asymptotic error caused by truncation of frequency domain and the fixed B . Finally, after $\omega > \frac{B}{2}$, the error increases as the artificial bandwidth B can no longer guarantee a sufficient sampling of frequency domain. According to the Nyquist–Shannon sampling theorem, we will set $B \geq 2\omega$. By comparing the errors for different bandwidths B in the interval where the errors do not vary much, we observe an asymptotic behavior of $\frac{1}{B}$. Therefore, we can conclude that, when solving the Helmholtz equation, the Hadamard integrator enjoys a frequency-dependent asymptotic convergence in the form of $O(\frac{1}{\omega^{1.5}}) + O(\frac{1}{B^{0.5}})$.

7 Conclusion

Based on the Kirchhoff-Huygens representation, Hadamard's ansatz and Babich's ansatz, we developed a novel butterfly-compressed Eulerian Hadamard integrator for solving the high-frequency wave equation in time and frequency domain. We derive the Eulerian formulations via the Fourier transform and utilize the butterfly algorithm to accelerate the resulting matrix-vector multiplication. The proposed integrator propagates wave fields beyond caustics implicitly and advance spatially overturning waves naturally, and it also enjoys quasi-linear computational complexity and memory usage. Once the integrator is constructed, it can simultaneously solve the time-domain wave equations with different initial conditions or the frequency-domain wave equations with different point-source locations in the computational domain. Numerical examples illustrate the accuracy and efficiency of the new integrators.

Compliance with Ethical Standards

Conflict of interest

On behalf of all authors, the corresponding author states that there is no conflict of interest.

Data Availability Statement

Data sets generated during the current study are available from the corresponding author on reasonable request.

Appendix A Computation of Singular Terms.

A.1 Frequency-space integral

Consider

$$I(t, \mathbf{x}_0; \mathbf{x}) = \int_0^{\Delta\omega} e^{-i\omega t} \hat{G}_0(\omega, \mathbf{x}_0; \mathbf{x}) d\omega \quad (8.1)$$

in the frequency-space integrals. Since the HKH propagator is short-time valid, both t and τ are bounded by a sufficiently small ΔT . In the numerical examples, we take $\Delta\omega = \frac{\pi}{2}$, $\Delta T = \frac{1}{8}$. The small arguments ωt and $\omega\tau$ allow us to use the Taylor expansion of $e^{-i\omega t}$ and polynomial approximation of Bessel functions. According to [1], we have the following polynomial approximations of Bessel functions $J_0(x)$ and $Y_0(x)$ when $0 < x < 3$,

$$J_0(x) = 1 - a_1\left(\frac{x}{3}\right)^2 + a_2\left(\frac{x}{3}\right)^4 + \epsilon, \quad |\epsilon| = O\left(\left(\frac{x}{3}\right)^6\right), \quad (8.2)$$

and

$$Y_0(x) = \frac{2}{\pi} \ln\left(\frac{x}{2}\right) J_0(x) + b_1 + b_2\left(\frac{x}{3}\right)^2 - b_3\left(\frac{x}{3}\right)^4 + \epsilon, \quad |\epsilon| = O\left(\left(\frac{x}{3}\right)^6\right), \quad (8.3)$$

where we denote

$$a_1 = 2.2499997, \quad a_2 = 1.2656208, \quad b_1 = 0.36746691, \quad b_2 = 0.60559366, \quad b_3 = 0.74350384.$$

Using the Taylor expansion of $e^{-i\omega t}$, we obtain

$$\begin{aligned} ie^{-i\omega t} H_0^1(\omega\tau) \approx & i\left(1 + i\omega t - \frac{\omega^2 t^2}{2} - \frac{i\omega^3 t^3}{6} + \frac{\omega^4 t^4}{24}\right) \left[\left(1 + \frac{2i}{\pi} \ln\left(\frac{\omega\tau}{2}\right)\right) \left(1 - a_1\left(\frac{\omega\tau}{3}\right)^2\right.\right. \\ & \left.\left.+ a_2\left(\frac{\omega\tau}{3}\right)^4\right) + ib_1 + ib_2\left(\frac{\omega\tau}{3}\right)^2 + ib_3\left(\frac{\omega\tau}{3}\right)^4\right]. \end{aligned} \quad (8.4)$$

Dropping higher-order terms above fifth order and the imaginary part, and calculating the definite integral over $[0, \Delta\omega]$, we obtain

$$\int_0^{\Delta\omega} e^{-i\omega t} \hat{G}_0(\omega, \mathbf{x}_0; \mathbf{x}) d\omega \approx \frac{\sqrt{\pi}}{2} v_0(L_1 - L_2), \quad (8.5)$$

where

$$\begin{aligned} L_1 \approx & \frac{1}{(\Delta\omega)\pi} \left\{ -2(\Delta\omega)^2 + 2 \frac{[(\Delta\omega)^4(72t^2 + 16a_1\tau^2)]}{648} - \frac{(\Delta\omega)^6(54t^4 + 72a_1t^2\tau^2 + 16a_2\tau^4)}{16200} \right. \\ & + (\Delta\omega)^2 \ln\left(\frac{(\Delta\omega)\tau}{2}\right) + \frac{(\Delta\omega)^6 \ln\left(\frac{(\Delta\omega)\tau}{2}\right)(54t^4 + 72a_1t^2\tau^2 + 16a_2\tau^4)}{3240} \\ & \left. - \frac{(\Delta\omega)^4 \ln\left(\frac{(\Delta\omega)\tau}{2}\right)(216t^2 + 48a_1\tau^2)}{648} \right\} - \frac{1}{(\Delta\omega)} [-b_1(\Delta\omega)^2 \\ & + \frac{(\Delta\omega)^4(108b_1t^2 - 24b_2\tau^2)}{648} + \frac{(\Delta\omega)^6(-27b_1t^4 + 36b_2t^2\tau^2 + 8b_3\tau^4)}{3240}], \end{aligned} \quad (8.6)$$

and

$$\begin{aligned} L_2 \approx & \int_0^{\Delta\omega} \left(\omega t - \frac{\omega^3 t^3}{6} + \frac{\omega^5 t^5}{120}\right) \left(1 - a_1\left(\frac{\omega\tau}{3}\right)^2 + a_2\left(\frac{\omega\tau}{3}\right)^4\right) d\omega \\ \approx & \int_0^{\Delta\omega} \omega t \left(1 - a_1\left(\frac{\omega\tau}{3}\right)^2 + a_2\left(\frac{\omega\tau}{3}\right)^4\right) - \frac{\omega^3 t^3}{6} \left(1 - a_1\left(\frac{\omega\tau}{3}\right)^2\right) + \frac{\omega^5 t^5}{120} d\omega \\ = & \int_0^{\Delta\omega} \omega t - \left(a_1 \frac{t\tau^2}{9} + \frac{t^3}{6}\right) \omega^3 + \left(a_2 \frac{t\tau^4}{81} + a_1 \frac{t^3\tau^2}{54} + \frac{t^5}{120}\right) \omega^5 d\omega \\ = & \frac{(\Delta\omega)^2 t}{2} - \left(a_1 \frac{t\tau^2}{9} + \frac{t^3}{6}\right) \frac{(\Delta\omega)^4}{4} + \left(a_2 \frac{t\tau^4}{81} + a_1 \frac{t^3\tau^2}{54} + \frac{t^5}{120}\right) \frac{(\Delta\omega)^6}{6}. \end{aligned} \quad (8.7)$$

A.2 Diagonal term of $I(t, \mathbf{x}_0; \mathbf{x})$

As shown in the appendix of [24], the integral of self-intersection term inside source cell c_j

$$\begin{aligned} \int_{c_j} \hat{G}_0(\omega_k, \mathbf{x}_0; \mathbf{x}) d\mathbf{x} \approx & \frac{i\sqrt{\pi}}{2} v_0(\mathbf{x}_0; \mathbf{x}_0) \frac{1}{(n_0\omega_k)^2} \left[8 \int_0^{\frac{\pi}{4}} \frac{hn_0\omega_k}{2 \cos \theta} H_1^{(1)}\left(\frac{hn_0\omega_k}{2 \cos \theta}\right) d\theta + 4i \right] \\ = & \frac{i}{4\nu_0 (n_0\omega_k)^2} \left[8 \int_0^{\frac{\pi}{4}} \frac{hn_0\omega_k}{2 \cos \theta} H_1^{(1)}\left(\frac{hn_0\omega_k}{2 \cos \theta}\right) d\theta + 4i \right], \end{aligned} \quad (8.8)$$

where $n_0 = n(\mathbf{x}_0)$, $\nu_0 = \nu(\mathbf{x}_0)$, and we use the initialization (3.9).

Now we consider self-intersection term of $I(t, \mathbf{x}_0; \mathbf{x})$. Starting from (8.8), we have

$$\begin{aligned}
\int_{c_j} I(t, \mathbf{x}_0; \mathbf{x}) d\mathbf{x} &= \int_0^{\Delta\omega} \frac{ie^{-i\omega t}}{4\nu_0(n_0\omega)^2} \left[8 \int_0^{\frac{\pi}{4}} \frac{hn_0\omega}{2\cos\theta} H_1^{(1)}\left(\frac{hn_0\omega}{2\cos\theta}\right) d\theta + 4i \right] d\omega \\
&= \int_0^{\frac{\pi}{4}} \int_0^{\Delta\omega} \frac{2ie^{-i\omega t}}{\nu_0(n_0\omega)^2} \left[\frac{hn_0\omega}{2\cos\theta} H_1^{(1)}\left(\frac{hn_0\omega}{2\cos\theta}\right) + \frac{2i}{\pi} \right] d\omega d\theta \\
&= \int_0^{\frac{\pi}{4}} \int_0^{\Delta\omega} \frac{ie^{-i\omega t} h^2}{2\nu_0 \cos^2\theta} \left(\frac{2\cos\theta}{hn_0\omega} \right)^2 \left[\frac{hn_0\omega}{2\cos\theta} H_1^{(1)}\left(\frac{hn_0\omega}{2\cos\theta}\right) + \frac{2i}{\pi} \right] d\omega d\theta \\
&\doteq S_1.
\end{aligned} \tag{8.9}$$

To handle $H_1^{(1)}(s) = J_1(s) + iY_1(s)$, we introduce the polynomial approximation of Bessel functions J_1 and Y_1 [1] when $0 < s < 3$,

$$\begin{aligned}
s^{-1}J_1(s) &= \frac{1}{2} - 0.56249985\left(\frac{s}{3}\right)^2 + 0.21093573\left(\frac{s}{3}\right)^4 - 0.03954289\left(\frac{s}{3}\right)^6 + 0.00443319\left(\frac{s}{3}\right)^8 \\
&\quad - 0.00031761\left(\frac{s}{3}\right)^{10} + 0.00001109\left(\frac{s}{3}\right)^{12} + \epsilon \quad |\epsilon| < 1.3 \times 10^{-8},
\end{aligned} \tag{8.10}$$

and

$$\begin{aligned}
sY_1(s) &= \frac{2}{\pi} s \ln\left(\frac{s}{2}\right) J_1(s) - \frac{2}{\pi} + 0.2212091\left(\frac{s}{3}\right)^2 + 2.1682709\left(\frac{s}{3}\right)^4 - 1.3164827\left(\frac{s}{3}\right)^6 \\
&\quad + 0.3123951\left(\frac{s}{3}\right)^8 - 0.0400976\left(\frac{s}{3}\right)^{10} + 0.0027873\left(\frac{s}{3}\right)^{12} + \epsilon, \quad |\epsilon| < 1.1 \times 10^{-7}.
\end{aligned} \tag{8.11}$$

Thus as $s = \frac{hn_0\omega}{2\cos\theta} \rightarrow 0$, we obtain

$$\begin{aligned}
\frac{1}{s^2} \left(sH_1^{(1)}(s) + \frac{2i}{\pi} \right) &= \frac{1}{s^2} \left[s(J_1(s) + iY_1(s)) + \frac{2i}{\pi} \right] \\
&= \frac{1}{s} J_1(s) + i \left(\frac{1}{s^2} \right) \left(sY_1(s) + \frac{2}{\pi} \right) \\
&\sim \frac{1}{2} + i \frac{1}{\pi} \ln\left(\frac{1}{2}s\right).
\end{aligned} \tag{8.12}$$

Dropping the high order terms, we have

$$s^{-1}J_1(s) = \frac{1}{2} - 0.56249985\left(\frac{s}{3}\right)^2 + 0.21093573\left(\frac{s}{3}\right)^4 \tag{8.13}$$

for the real part and

$$\frac{1}{s^2} \left(sY_1(s) + \frac{2}{\pi} \right) = \frac{2}{\pi} \ln\left(\frac{s}{2}\right) s^{-1}J_1(s) + \frac{1}{s^2} \left(0.2212091\left(\frac{s}{3}\right)^2 + 2.1682709\left(\frac{s}{3}\right)^4 - 0.03954289\left(\frac{s}{3}\right)^6 \right) \tag{8.14}$$

for the imaginary part. The singularity appearing in the first term of (8.14) can be removed in the following way,

$$\begin{aligned}
S_1 &= \int_0^{\frac{\pi}{4}} \frac{ih^2}{2\nu_0 \cos^2\theta} \int_0^{\Delta\omega} e^{-i\omega t} \left(\frac{2\cos\theta}{hn_0\omega} \right)^2 \left[\frac{hn_0\omega}{2\cos\theta} H_1^{(1)}\left(\frac{hn_0\omega}{2\cos\theta}\right) + \frac{2i}{\pi} \right] d\omega d\theta \\
&= \int_0^{\frac{\pi}{4}} \frac{ih^2}{2\nu_0 \cos^2\theta} \int_0^{\Delta\omega} e^{-i\omega t} \left(\frac{2\cos\theta}{hn_0\omega} \right)^2 \left[\frac{hn_0\omega}{2\cos\theta} H_1^{(1)}\left(\frac{hn_0\omega}{2\cos\theta}\right) + \frac{2i}{\pi} \right] d\omega d\theta \\
&\quad - \frac{i}{\pi} \ln\left(\frac{hn_0\omega}{4\cos\theta}\right) d\omega d\theta + \int_0^{\frac{\pi}{4}} \int_0^{\Delta\omega} \frac{i^2 h^2}{2\nu_0 \cos^2\theta} \frac{1}{\pi} \ln\left(\frac{hn_0\omega}{4\cos\theta}\right) d\omega d\theta,
\end{aligned} \tag{8.15}$$

where the last singular term in (8.15) can be handled as

$$\begin{aligned}
&\int_0^{\frac{\pi}{4}} \int_0^{\Delta\omega} \frac{i^2 h^2}{2\nu_0 \cos^2\theta} \frac{1}{\pi} \ln\left(\frac{hn_0\omega}{4\cos\theta}\right) d\omega d\theta \\
&= -\frac{2h^2}{\pi\nu_0} \int_0^{\frac{\pi}{4}} \int_0^{\Delta\omega} \frac{1}{\cos^2\theta} \ln\left(\frac{hn_0\omega}{4\cos\theta}\right) d\omega d\theta \\
&= -\frac{2h^2}{\pi\nu_0} \int_0^{\frac{\pi}{4}} \int_0^{\Delta\omega} \frac{1}{\cos^2\theta} [\ln(hn_0\omega) - \ln(4\cos\theta)] d\omega d\theta \\
&= -\frac{2h^2}{\pi\nu_0} \int_0^{\frac{\pi}{4}} \frac{1}{\cos^2\theta} [\Delta\omega (\ln(\frac{hn_0\Delta\omega}{4\cos\theta}) - 1)] d\theta.
\end{aligned} \tag{8.16}$$

A.3 Diagonal term of $\hat{G}_0(\omega, \mathbf{x}_0; \mathbf{x}) \left(\frac{\partial}{\tau \partial \tau} \right) \left(\frac{u^k}{v_0} \right)$

Consider the self-intersection terms of (4.28) with non-zero ω in cell c_j , where n and non-singular ingredients are taken as constant. We state that

$$S_2 \doteq \int_{c_j} \hat{G}_0(\omega, \mathbf{x}_0; \mathbf{x}) \left(\frac{\partial}{\tau \partial \tau} \right) \left(\frac{u^k}{v_0} \right) d\mathbf{x} = 0, \quad k = 1, 2, \quad (8.17)$$

which implies that the self-intersection term is zero.

Note when $n = n_0$,

$$\frac{\partial}{\partial \tau} = c^2 \nabla \tau \cdot \nabla = \frac{1}{n_0} (\cos \theta, \sin \theta) \cdot \nabla, \quad (8.18)$$

where θ is the take-off angle, which is consistent with that in the polar coordinate transformation when $n = n_0$. And

$$\hat{G}_0(\omega, \mathbf{x}_0; \mathbf{x}) = \frac{i}{4\nu_0} H_0^1(\omega n_0 |\mathbf{x} - \mathbf{x}_0|), \quad (8.19)$$

which is a radial function. Then we can obtain (8.17) by symmetry. Actually, we can divide the cell c_j into four parts

$$\begin{cases} c_j^1 : \theta \in [-\frac{\pi}{4}, \frac{\pi}{4}], r \in [0, \frac{h}{2 \cos(\theta)}], \\ c_j^2 : \theta \in [\frac{\pi}{4}, \frac{3\pi}{4}], r \in [0, \frac{h}{2 \sin(\theta)}], \\ c_j^3 : \theta \in [\frac{3\pi}{4}, \frac{5\pi}{4}], r \in [0, -\frac{h}{2 \cos(\theta)}], \\ c_j^4 : \theta \in [\frac{5\pi}{4}, \frac{7\pi}{4}], r \in [0, -\frac{h}{2 \sin(\theta)}]. \end{cases} \quad (8.20)$$

Now we use the polar coordinate transformation in (8.17), yielding

$$\begin{aligned} S_2 &= \int \int \frac{i}{4\nu_0} H_0^1(\omega n_0 |\mathbf{x} - \mathbf{x}_0|) \frac{1}{n_0} (\cos \theta, \sin \theta) \cdot \nabla \left(\frac{u^k}{v_0} \right) \frac{1}{n_0 |\mathbf{x} - \mathbf{x}_0|} |\mathbf{x} - \mathbf{x}_0| dr d\theta \\ &= \frac{i}{4\rho_j} \left(\int_{c_j^1} + \int_{c_j^2} + \int_{c_j^3} + \int_{c_j^4} \right) H_0^1(\omega n_0 |\mathbf{x} - \mathbf{x}_0|) (\cos \theta, \sin \theta) \cdot \nabla \left(\frac{u^k}{v_0} \right) dr d\theta \\ &\doteq S_{2,1} + S_{2,2} + S_{2,3} + S_{2,4}. \end{aligned} \quad (8.21)$$

Substituting $\xi = \theta + \pi$, it is easy to verify that

$$S_{2,1} + S_{2,3} = 0, \quad S_{2,2} + S_{2,4} = 0.$$

That is, $S_2 = 0$.

References

1. Abramowitz, M., Stegun, I.A.: Handbook of mathematical functions. Dover Publications, Inc., New York. (1965)
2. Babich, V.M.: The short wave asymptotic form of the solution for the problem of a point source in an inhomogeneous medium. *USSR Computational Mathematics and Mathematical Physics* **5**(5), 247–251 (1965)
3. Babuška, I.M., Sauter, S.A.: Is the pollution effect of the FEM avoidable for the Helmholtz equation considering high wave numbers? *SIAM Review* **42**, 451–484 (2000)
4. Bao, G., Lai, J., Qian, J.: Fast multiscale Gaussian beam methods for wave equations in bounded domains. *J. Comput. Phys.* **261**, 36–64 (2014)
5. Bayliss, A., Goldstein, C.I., Turkel, E.: On accuracy conditions for the numerical computation of waves. *J. Comput. Phys.* **59**, 396–404 (1985)
6. Candes, E., Demanet, L., Ying, L.: A fast butterfly algorithm for the computation of Fourier integral operators. *SIAM Multiscale Model. Simul.* **7**, 1727–1750 (2009)
7. Courant, R., Hilbert, D.: Methods of mathematical physics, vol. II. John Wiley-Sons (1962)
8. Fomel, S., Luo, S., Zhao, H.K.: Fast sweeping method for the factored eikonal equation. *J. Comput. Phys.* **228**, 6440–6455 (2009)
9. Gelfand, I., Shilov, G.: Generalized Functions, vol. 1. Academic Press, New York and London (1964)
10. Hadamard, J.: Lectures on Cauchy's Problem in Linear Partial Differential Equations. Yale University Press; (reprinted Dover Publications, New York 1952) (1923)
11. Ho, K., Leung, S., Qian, J.: Fast Huygens sweeping methods for a class of nonlocal Schrodinger equations. *J. Sci. Comput.* **88**, 54 (2021)

12. Jiang, G.S., Peng, D.: Weighted ENO schemes for Hamilton-Jacobi equations. *SIAM J. Sci. Comput.* **21**, 2126–2143 (2000)
13. Kao, C.Y., Osher, S.J., Qian, J.: Lax-Friedrichs sweeping schemes for static Hamilton-Jacobi equations. *J. Comput. Phys.* **196**, 367–391 (2004)
14. Kwan, W., Leung, S., Wang, X.P., Qian, J.: A fast Huygens sweeping method for capturing paraxial multi-color optical self-focusing in nematic liquid crystals. *J. Comput. Phys.* **348**, 108–138 (2017)
15. Leung, S., Qian, J.: Eulerian Gaussian beam methods for Schrödinger equations in the semi-classical regime. *J. Comput. Phys.* **228**, 2951–2977 (2009)
16. Leung, S., Qian, J.: The backward phase flow and FBI-transform-based Eulerian Gaussian beams for the Schrödinger equation. *J. Comput. Phys.* **229**, 8888–8917 (2010)
17. Leung, S., Qian, J., Burrridge, R.: Eulerian Gaussian beams for high frequency wave propagation. *Geophysics* **72**, SM61–SM76 (2007)
18. Leung, S., Qian, J., Serna, S.: Fast Huygens sweeping methods for Schrodinger equations in the semiclassical regime. *Methods Appl. Anal.* **21**, 031–066 (2014)
19. Leung, S., Zhao, H.K.: Gaussian beam summation for diffraction in inhomogeneous media based on the grid based particle method. *Comm. in Comp. Phys.* **8**, 758–796 (2010)
20. Li, Y., Yang, H.: Interpolative butterfly factorization. *SIAM Journal on Scientific Computing* **39**(2), A503–A531 (2017)
21. Li, Y., Yang, H., Martin, E.R., Ho, K.L., Ying, L.: Butterfly factorization. *Multiscale Modeling & Simulation* **13**(2), 714–732 (2015)
22. Liu, X.D., Osher, S.J., Chan, T.: Weighted Essentially NonOscillatory schemes. *J. Comput. Phys.* **115**, 200–212 (1994)
23. Liu, Y., Guo, H., Michielssen, E.: An hss matrix-inspired butterfly-based direct solver for analyzing scattering from two-dimensional objects. *IEEE Antennas and Wireless Propagation Letters* **16**, 1179–1183 (2016)
24. Liu, Y., Song, J., Burrridge, R., Qian, J.: A fast butterfly-compressed Hadamard-Babich integrator for high-frequency Helmholtz equations in inhomogeneous media with arbitrary sources. *SIAM Multiscale Model. Simul.* **21**, 269–308 (2023)
25. Liu, Y., Xing, X., Guo, H., Michielssen, E., Ghysels, P., Li, X.S.: Butterfly factorization via randomized matrix-vector multiplications. *SIAM J. Sci. Comput.* **43**, A883–A907 (2021)
26. Lu, W., Qian, J., Burrridge, R.: Babich-like ansatz for three-dimensional point-source Maxwell’s equations in an inhomogeneous medium at high frequencies. *SIAM J. Multiscale Model. Simul.* **14**(3), 1089–1122 (2016)
27. Lu, W., Qian, J., Burrridge, R.: Babich’s expansion and the fast Huygens sweeping method for the Helmholtz wave equation at high frequencies. *J. Comput. Phys.* **313**, 478–510 (2016)
28. Lu, W., Qian, J., Burrridge, R.: Extending Babich’s ansatz for point-source Maxwell’s equations using Hadamard’s method. *SIAM J. Multiscale Model. Simul.* **16**, 727–751 (2018)
29. Luo, S., Qian, J., Burrridge, R.: Fast Huygens sweeping methods for Helmholtz equations in inhomogeneous media in the high frequency regime. *J. Comput. Phys.* **270**, 378–401 (2014)
30. Luo, S., Qian, J., Burrridge, R.: High-order factorization based high-order hybrid fast sweeping methods for point-source eikonal equations. *SIAM J. Numer. Anal.* **52**, 23–44 (2014)
31. Michielssen, E., Boag, A.: A multilevel matrix decomposition algorithm for analyzing scattering from large structures. *IEEE Transactions on Antennas and Propagation* **44**(8), 1086–1093 (1996)
32. Osher, S.J., Shu, C.W.: High-order Essentially NonOscillatory schemes for Hamilton-Jacobi equations. *SIAM J. Numer. Anal.* **28**, 907–922 (1991)
33. Qian, J., Lu, W., Yuan, L., Luo, S., Burrridge, R.: Eulerian geometrical optics and fast Huygens sweeping methods for three-dimensional time-harmonic high-frequency Maxwell’s equations in inhomogeneous media. *SIAM J. Multiscale Modeling and Simulation* **16**, 595–636 (2016)
34. Qian, J., Song, J.: Fast multiscale Gaussian beam method for three-dimensional elastic wave equations in bounded domains. *SIAM J. Numer. Anal.* **59**, 2536–2570 (2021)
35. Qian, J., Song, J., Lu, W., Burrridge, R.: Hadamard-Babich ansatz for point-source elastic wave equations in variable media at high frequencies. *SIAM Multiscale Model. Simul.* **19**, 46–86 (2021)
36. Qian, J., Song, J., Lu, W., Burrridge, R.: Truncated Hadamard-Babich ansatz and fast Huygens sweeping methods for time-harmonic high-frequency elastic wave equations in inhomogeneous media. *Minimax Theory and its Applications* **8**, 171–212 (2023)
37. Qian, J., Symes, W.W.: An adaptive finite difference method for traveltime and amplitude. *Geophysics* **67**, 167–176 (2002)
38. Qian, J., Ying, L.: Fast Gaussian wavepacket transforms and Gaussian beams for the Schrödinger equation. *J. Comput. Phys.* **229**, 7848–7873 (2010)
39. Qian, J., Ying, L.: Fast multiscale Gaussian wavepacket transforms and multiscale Gaussian beams for the wave equation. *SIAM J. Multiscale Modeling and Simulation* **8**, 1803–1837 (2010)
40. Qian, J., Yuan, L., Liu, Y., Luo, S., Burrridge, R.: Babich’s expansion and high-order Eulerian asymptotics for point-source Helmholtz equations. *Journal of Scientific Computing* **67**, 883–908 (2016)
41. Symes, W.W., Qian, J.: A slowness matching Eulerian method for multivalued solutions of eikonal equations. *J. Sci. Comp.* **19**, 501–526 (2003)
42. Tanushev, N., Engquist, B., Tsai, R.: Gaussian beam decomposition of high frequency wave fields. *J. Comput. Phys.* **228**, 8856–8871 (2009)
43. Tanushev, N., Qian, J., Ralston, J.: Mountain waves and Gaussian beams. *SIAM J. Multiscale Modeling and Simulation* **6**, 688–709 (2007)
44. Wei, Y., Cheng, J., Burrridge, R., Qian, J.: Hadamard integrator for time-dependent wave equations: Lagrangian formulation via ray tracing. *Journal of Computational Physics* **497**, 112637 (2024)
45. Zhang, L., Rector, J.W., Hoversten, G.M.: Eikonal solver in the celerity domain. *Geophys. J. Internat.* **162**, 1–8 (2005)
46. Zhao, H.K.: Fast sweeping method for eikonal equations. *Math. Comp.* **74**, 603–627 (2005)